Revision 2

Kyanite preserves prograde and retrograde metamorphic events as revealed by cathodoluminescence, geochemistry, and crystallographic orientation

Running title: Metamorphic events preserved within kyanite

Emily M. Peterman[1]*

Michael J. Jercinovic[2]

Rachel J. Beane[1]

Cameron B. de Wet[1,3]

[1] Department of Earth & Oceanographic Science; Bowdoin College; 6800 College Station; Brunswick, ME 04011, USA

[2] Department of Geosciences; University of Massachusetts-Amherst; 627 N. Pleasant St.; Amherst, MA 01003, USA

[3] Department of Earth and Environmental Sciences; Vanderbilt University; 5726 Stevenson Center; Nashville, TN 37240, USA

*corresponding author: epeterman@bowdoin.edu

ABSTRACT

Cathodoluminescence (CL) images of kyanite reveal several internal textures, including sector zoning, oscillatory zoning, and cross-cutting relationships among different domains. Many textures observed in kyanite correspond to discrete events, thereby connecting kyanite textures to the pressure-temperature (*P-T*) history of the rock. To evaluate the record of metamorphism preserved by kyanite, metapelites were selected from three different orogens that reflect *P-T* conditions ranging from amphibolite to ultrahigh-pressure (UH*P*) facies. Cross-correlation of variations in CL intensity, chemistry, and crystal orientation within kyanite indicate the following findings. First, the preservation of original growth zones in kyanite from poly-metamorphic rocks demonstrates that growth zoning in kyanite persists through metamorphic events and is not erased by diffusion or complete recrystallization. In some samples, kyanite retains evidence of its reaction history during growth. Second, measured changes in absolute crystallographic orientation do not correspond with changes in CL intensity in any of the measured samples, including kyanite twins. Third, both kink banding and undulatory extinction are present across all samples, consistent with rotation about <010> in the (100)[001] slip system. Kyanite from (U)H*P* samples exhibits higher amplitude undulations than kyanite from lower grade lithologies, suggesting that crystallographic orientation data may provide complementary insight about deformation along the *P-T* path. Fourth, specific CL and trace element signatures in kyanite can be correlated with discrete metamorphic histories; yet CL intensity and color are affected by multiple elements, not a single controlling element. In sum, multiple generations of kyanite can be identified by careful cross-correlation of CL and geochemical data, and when combined with crystal orientation data, kyanite provides a robust record of a rock's *P-T* evolution.

KEYWORDS: kyanite, cathodoluminescence, EPMA, EBSD, metamorphism

INTRODUCTION

Kyanite is a common, chemically simple Al_2SiO_5 polymorph that has long been used as an index mineral for demarcating metamorphic grade (Barrow, 1893). Early work readily identified kyanite as the high-pressure polymorph of the aluminosilicates (Miyashiro, 1949; Clark et al., 1957). However, due to its relatively broad stability field and simple composition, the use of kyanite for determining a rock's metamorphic history has been limited. Instead, the record of metamorphism is generally extracted from compositionally variable phases such as garnet, plagioclase, biotite, and amphibole (e.g., Ferry & Spear, 1978), because the well-documented effects of pressure and temperature on exchange vectors among these phases readily facilitate interpretation of a rock's pressure-temperature (*P-T*) history. A classic example is the reaction:

garnet → aluminosilicate + quartz + plagioclase

wherein exchange between garnet and plagioclase is used to quantify pressure (e.g., Ghent, 1976; Holdaway, 2000; Newton & Haselton, 1981). Quartz and an aluminosilicate are required for the reaction, but they are irrelevant for thermodynamic calculations because their activities are so close to 1.0. However, a significant body of work on quartz, has shown that quartz preserves information about the conditions of recrystallization. For example, Ti concentrations in quartz correlate with the temperature (and pressure) of (re)crystallization (Ashley et al., 2013; Grujic et al., 2011; Huang & Audétat, 2012; Kidder et al., 2013; Nachlas et al., 2014; Ostapenko et al., 1987, 2007; Peterman & Grove, 2010; Thomas et al., 2010, 2015; Wark & Watson, 2006). Microstructural analysis of quartz provides constraints on the metamorphic conditions of quartz recrystallization (e.g., Law, 2014; Passchier & Trouw, 2005; Stipp et al., 2002). We hypothesize that kyanite may similarly preserve information regarding recrystallization and metamorphic reactions.

The existing literature on kyanite trace element geochemistry suggests that kyanite has the potential to preserve aspects of its metamorphic history. The trace elements Fe, Ti, V, and Cr are common

in kyanite (Albee & Chodos, 1969; Chinner et al., 1969; Deer et al., 1997; Herz & Dutra, 1964; Neiva, 1984; Pearson & Shaw, 1960) and may be linked to the origin of the protolith (Müller et al., 2016) or inherited from the phase(s) overprinted by kyanite (Yang & Rivers, 2001). Furthermore, variations in trace element concentrations can affect the macroscopic color of kyanite (e.g., Chadwick & Rossman, 2009; Faye & Nickel, 1969 and references therein; Owens & Dickerson, 2001; Tarantola et al., 2019). Recent studies suggest that Fe concentrations vary as a function of oxygen fugacity during crystallization (Müller et al., 2106; Tarantola et al., 2019) and that concentrations of Ti may correlate with increased temperatures during metamorphism (Kendrick & Indares, 2018; Müller et al., 2016), depending on the activity of Ti. Cr concentrations may correlate with temperature (Kendrick & Indares, 2018; Müller et al., 2016), but are likely controlled by the availability of Cr (Yang & Rivers, 2001). Results from laboratory experiments on mafic bulk compositions suggest that kyanite can incorporate significant concentrations of P during subduction to ultrahigh-pressure (UH*P*) conditions (up to 0.24 wt %; Konzett, 2016). In some cases, *in situ* analyses can link compositional domains to metamorphic reactions, thereby relating kyanite growth or decomposition to a rock's *P-T* history (Kendrick & Indares, 2018). These studies suggest that kyanite may record a robust history of metamorphism.

Cathodoluminescence (CL) imaging reveals textures within minerals that correlate with geologic events. As shown by the extensive literature on zircon (e.g., Corfu et al., 2003; Hanchar & Miller, 1993; Rubatto, 2017; Taylor et al., 2016) and quartz (Götze et al., 2001, and references therein; Rusk et al., 2008; Wark & Spear, 2005; Wark & Watson, 2006), multiple generations of mineral growth, chemical reactions, and deformation may be identified using CL images (e.g., Boggs & Krinsley, 2006; Götze & Kempe, 2008; Götze et al., 2013; Schertl et al., 2004; Sullivan and Peterman, 2017; Wiebe et al., 2007). Similarly, kyanite preserves distinct internal textures evident in CL (**Fig. 1**), including sector zoning, oscillatory zoning, and patchy domains. Most kyanite grains preserve evidence of cross-cutting relationships among different textural domains (Götze et al., 2013; Horkley et al., 2013; Kendrick & Indares, 2018; Müller et al., 2016;

Schertl et al., 2004). Trace element variation explains much of the observed variation in CL intensity and color: Cr^{3+} enrichment drives much of the red luminescence (centered at 734 nm; Müller et al., 2016) and Ti^{4+} concentrations correlate with blue luminescence at 485 nm (Gaft & Panczer, 2013; Götze et al., 2013; Habermann, 2002; Horkley et al., 2013; Müller et al., 2012; Schertl et al., 2004; Wojtowicz, 1991; Wojtowicz et al., 1991). Although variations in the concentrations of Cr and Ti correlate well with observed color and intensity shifts (Müller et al., 2016), there are several examples where these trace elements do not fully explain the CL emission. The CL signal is quenched in kyanite with Fe >3200 ppm (Müller et al., 2016), but lower concentrations appear to correlate with blue or green CL emission (Horkley et al., 2013). In some cases, V, Li and Ga appear to affect CL intensity (Kendrick & Indares, 2018; Horkley et al., 2013), but each element's effects are difficult to isolate and may be non-systematic. Some studies suggest that variations in crystallographic orientation affect CL intensity (Kendrick & Indares, 2018; Götze et al., 2013; Schertl et al., 2004) and other studies show that radiation damage sourced from adjacent phases affects CL emission (Rezvukhina et al., 2019).

In this contribution, we systematically assess the effects of trace element composition and crystallographic orientation on CL emission in kyanite to evaluate the metamorphic record preserved within kyanite. We examined kyanite metamorphosed at amphibolite facies to ultrahigh-pressure (UH*P*) conditions in three different orogens. We focus on garnet-kyanite-bearing metapelites for which the *P-T* history is largely understood, as that provides a framework for understanding the significance of variations in CL, geochemistry, and crystallographic orientation. Our results show that kyanite can preserve a rich history, even in samples where the matrix was recrystallized. Because recrystallization commonly overprints the prograde history, kyanite's potential to preserve multiple stages of metamorphism is significant. The record provided by kyanite thus complements the history documented by other phases and may provide new insights regarding the metamorphic history of these rocks.

GEOLOGIC BACKGROUND OF THE SAMPLES

Kokchetav Massif, Kazakhstan

Samples of the Kokchetav whiteschist (K-18) were collected south of Lake Zheltau in the Kulet region from the UH*P* metamorphic unit II of the Kokchetav Massif, as previously described by Beane & Field (2007). Peak conditions for the whiteschist are 3.5 GPa, 720–760°C (Parkinson, 2000). As determined from the associated eclogites, subduction occurred 537–527 Ma, followed by exhumation and recrystallization at crustal depths by 500 Ma (Zhang et al., 2012). The equilibrium assemblage for the whiteschist is kyanite + garnet + talc + phengite + coesite. In thin section, kyanite grains up to 10 mm in length display a weak shape preferred alignment that corresponds to a strong foliation defined by talc and phengite. Raman spectroscopic imaging has revealed "graphite, rutile, phengite, quartz, coesite, and monazite" inclusions within Kulet kyanite (Rezvukhina et al., 2019). Most kyanite porphyroblasts are euhedral and exhibit undulose extinction. A few kyanite blades contain one or more kink bands. Kyanite grains included within garnet are rounded with no undulose extinction or kink bands.

Rhodope Metamorphic Complex, Eastern Greece

The Rhodope Metamorphic Complex of eastern Greece and southern Bulgaria is divided into four main tectonic units: Lower, Middle, Upper, and Uppermost Allochthons (Janák et al., 2011). The Middle and Upper Allochthons were thrust southwest over the Lower Allochthon during Alpine convergence, producing a nappe stack (Janák et al., 2011). Diamond-bearing metapelites from both the Upper and Middle Allochthons indicate peak metamorphism at >4.5 GPa, ~800°C (e.g., Krenn et al., 2010; Mposkos et al., 2001). Although the number of UH*P* ± H*P* events remains disputed (Janák et al., 2011; Kirchenbaur et al., 2012; Krenn et al., 2010, 2011; Liati, 2005; Liati et al., 2016), there is general consensus that peak pressures were attained by c. 180 Ma and that the Middle Allochthon metapelites near Xanthi

were equilibrated at granulite to upper amphibolite facies 149–144 Ma (Krenn et al., 2010; Liati et al., 2016; Peterman et al., 2016a; Peterman et al., 2019). Lower grade metamorphic events associated with exhumation post-date these two major events.

Metapelites collected from Xanthi (57074; 57081; OS18-011; W17-001C) contain mm- to cm-scale euhedral to subhedral kyanite; the rock locally contains >40% kyanite. Matrix kyanite commonly displays a shape-preferred alignment to the main fabric, which is defined by recrystallized quartz ribbons, phlogopite, muscovite, and chlorite. Most kyanite are surrounded by quartz, phlogopite, and/or muscovite. Many kyanite exhibit undulatory extinction and one or more kink bands. Kyanite included within garnet do not exhibit undulatory extinction or kink bands; these grains are commonly oblique to the matrix fabric.

The Northern Appalachians

The Northern Appalachians is a multiphase accretionary orogen produced from Devonian to Carboniferous time. The protracted Acadian orogeny involved west-directed thrusting of Devonian metasediments over the previously accreted Taconian arc and a dome stage characterized by regional metamorphism at 500–650°C, 8–11 kbar (Kohn & Spear, 1990; Menard & Spear, 1994; Spear et al., 2002; Karabinos et al., 1998, 2017; Macdonald et al., 2014). U–Pb monazite dates span from 400 to 365 Ma (Cheney et al., 2006; Lanzirotti & Hanson, 1995; Peterman et al., 2014; Pyle et al., 2005), which is consistent with zircon (Peterman et al., 2016b) and $^{40}Ar/^{39}Ar$ dates (Armstrong et al., 1992). Garnet growth occurred c. 380 Ma (Gatewood et al., 2015; Vance & Holland, 1993). Within the Northern Appalachians, localized bodies were metamorphosed at UH*T* conditions (Ague & Eckert, 2012; Ague et al., 2013; Keller et al., 2020); evidence of UH*P* metamorphism also has been proposed (Snoeyenbos, 2011; Peterman et al., 2016b; Keller et al., 2020), but neither coesite nor diamond have been reported in the Northern Appalachians.

Samples of metapelites from the Northern Appalachians, USA, were collected from the Cobble Mountain Formation, the Gassetts Schist, the Straits Schist, and the Slashers Ledges Formation.

Cobble Mountain Formation

The Cobble Mountain Formation in Massachusetts is a quartzofeldspathic schist (Karabinos et al., 2017). Samples for this study crop out along the western margin of the Goshen Dome, which is a tectonic window through an Acadian thrust sheet (Hatch & Warren, 1981). Here the formation comprises restitic garnet-kyanite schists with lenses of boudinaged migmatitic garnet amphibolite and retrogressed eclogite blocks (Peterman et al., 2016b). The mineralogy and texture of the schist indicate re-equilibration at upper amphibolite facies conditions (12–14 kbar, 725°C). Although no coesite nor diamond has been observed, the trace element geochemistry of the garnet megacrysts and the oriented inclusion suite (apatite, rutile, quartz) within garnet megacrysts suggest a potential UH*P* origin (see discussion in Peterman et al., 2016b).

The metapelitic schist examined in this study (G12B) consists of garnet + kyanite + cordierite + quartz + plagioclase + phlogopite + chlorite + rutile. Kyanite ranges from a few mm to a few cm and exhibits three different textures: (1) poikiloblastic, cm-scale grains with embayed margins, surrounded by cordierite or quartz + phlogopite; (2) deformed cm-scale grains with short-wavelength undulatory extinction ± kink bands; and (3) fragments of largely decomposed cm-scale porphyroblasts rimmed by cordierite. Most kyanite grains contain abundant rutile; some also include apatite, monazite, zircon, or quartz. Elongate kyanite is preferentially aligned with the foliation, which is defined by phlogopite + chlorite. Some phlogopite grains contain oriented rutile needles ~10 μm. Garnet porphyroblasts measure 0.5 to 4 cm in diameter, exhibit concentric compositional zoning, and contain oriented rutile + apatite inclusions with disseminated zircon grains <10 μm; most porphyroblasts exhibit resorbed margins.

Gassetts Schist

The Gassetts Schist is an aluminous schist of the Cambrian Cavendish Formation that crops out along the western margin of the Chester-Athens Dome near Gassetts, Vermont. Estimates of the *P-T*-t path indicate garnet growth with increasing temperature and following a clockwise decompression path from 540°C, 9.7 kbar to 635°C, 7.2 kbar; Sm-Nd garnet-whole rock ages indicate garnet growth at 380 Ma (Vance & Holland, 1993). Recent work from the nearby Townshend Dam locality concluded that garnet grew during a loading and heating P-T path (Dragovic et al., 2018) whereas Spear and Wolfe (2020) used quartz-in-garnet barometry to conclude that garnet grew nearly isothermally and isobarically. In the sample examined in this study (P-84), elongate kyanite is oriented parallel to the schistose fabric, which is defined by muscovite + biotite ± late chlorite. A weak crenulation cleavage is observed in portions of the section. Larger kyanite grains exhibit weak, low amplitude undulose extinction; no kink bands are evident. Millimeter- to sub-mm kyanite is euhedral to subhedral and intergrown with staurolite and muscovite. Many kyanite grains contain rounded rutile inclusions.

Straits Schist

The Straits Schist, correlative with the Goshen Formation in western Massachusetts, is a distinctive rusty-weathering garnet-kyanite-bearing crenulated graphitic schist interlayered with more quartzofeldspathic domains (Hibbard et al., 2007; Stanley, 1964). These rocks record peak conditions of 700 ± 50°C, 9 ± 1 kbar (Lanzirotti & Hanson, 1995; Ramirez et al., 1996). The coarse-grained sample examined here (P-1156) was collected from western Connecticut and is dominated by mm- to cm-scale quartz + plagioclase + K-feldspar + biotite + kyanite with minor garnet, staurolite, muscovite, sillimanite, and rutile. Large portions of the thin section are graphitic with minor Fe sulfides; sericite alteration is common. Despite abundant sheet silicates, this sample does not exhibit a well-developed foliation. Large

(cm-scale) kyanite blades are abundant in the sample, and most are surrounded by muscovite. A few grains have weak undulose extinction and/or kink bands, but these features are not common to most grains; a few grains also exhibit twinning. Many kyanite grains contain anhedral rutile; some also contain zircon, muscovite, or monazite. Opaque inclusions, where present, are found along kyanite cleavage planes.

Slashers Ledges Formation

The Slashers Ledges Formation crops out in northern Connecticut and is subdivided into two members: a kyanite schist and a rusty-weathering schist (Stanley, 1964). The kyanite schist member is characterized by 10–20 cm blades and contains small porphyroblasts of magnetite, garnet and plagioclase (Stanley, 1964). Correlated with the Rowe Schist (Stanley, 1975), the Slashers Ledge Formation is interpreted as an accretionary wedge that formed off the continental shelf of Laurentia and was metamorphosed and thrust westward onto the Laurentian margin during the mid-Ordovician closure of the Taconic seaway (Karabinos et al., 2017; Macdonald et al., 2014). Thermobarometry of pelitic schists from the Rowe belt in western Connecticut indicates peak conditions of ~8 kbar, 575 ± 25°C (Dietsch, 1989; Hames et al., 1989).

The sample examined in this study (P-1158) exhibits a well-developed schistosity defined by muscovite + biotite. Elongate kyanite grains up to a few cm in length are parallel to the dominant fabric and contain abundant inclusions of sub-mm garnet, quartz, biotite, ilmenite, apatite, and graphite. Some kyanite grains show minor resorption along the margins and a few grains exhibit weak undulose extinction and/or twinning. Plagioclase feldspar contains abundant aligned inclusions of muscovite, biotite, and ilmenite that define a fabric dominantly parallel to the schistosity. In some plagioclase grains, the inclusions define a fold pattern oblique to the schistosity.

METHODS

SEM-CL

Cathodoluminescence images were collected using the Tescan Color CL detector on the Tescan VEGA3 scanning electron microscope (SEM) at Bowdoin College. The Tescan Color CL detector is sensitive in the range of 350 to 850 nm and can be operated in either panchromatic mode or Color CL mode. In Color CL mode, the signal is split into red, green and blue channels using dichroic filters and each channel can be examined independently or recombined to produce a composite color image (**Fig. 1**). Because changes in CL emission are easier to observe in the composite color images, we have elected to show these; additional figures documenting individual channel data are provided in the **Supplementary Materials**.

To determine the optimal analytical settings, we experimented with operating conditions (voltage, current, working distance, scan speed), panchromatic vs. ColorCL mode, detector brightness and contrast, and image parameters (gamma). As with quartz (Spear & Wark, 2009), beam damage and surface contamination can affect the luminescence of kyanite; therefore, beam parameters were optimized on sacrificial grains prior to imaging the grains presented here. Empirical results from our laboratory indicate that kyanite is optimally imaged at a working distance of 15.5 to 17 mm with an 18 kV, 1–3 nA beam. For most kyanite grains, a scan speed of 0.1 ms/pxl yielded optimal images; kyanite with apatite inclusions were imaged at 1 ms/pxl to minimize the streaking associated with apatite CL emission. For grains >0.5 cm, we used the Tescan large area mapping tool to acquire and stitch CL images into a panorama. Settings for brightness and contrast were determined by "black balancing" the image. Following a similar approach as white balancing in photography, we black balanced the acquisition parameters by centering the beam on a non-luminescent portion of the thin section and adjusting the brightness and contrast settings such that all peaks (red, green, and blue) overlap near the origin of the image histogram, thereby eliminating any apparent emission from non-luminescence minerals. We then

focused the beam on a kyanite grain and made minor adjustments to gamma (0.8–1.5) to ensure that textural features within the grain were evident. When using the same beam and image optimization parameters during the same analytical session, the CL color was reproducible.

EPMA

Compositional maps and quantitative point analyses of trace element concentrations in kyanite were collected on the CAMECA SX-UltraChron electron microprobe at the University of Massachusetts - Amherst. Mapping was done at 15 kV and 800 nA with 200ms pixel dwell time. Initial quantitative trace element analyses were performed at 20 kV, 200 nA using 540 second count times; subsequent analyses were conducted at 20 kV, 300nA, with 600 second count times. A fixed-concentration kyanite major element composition was assumed. Trace elements analyzed include: Ti, Zr, Mn, Cr, S, Ga, V, Cd, Ge, Fe, Mg, and P. TAP, large and very large PET (LPET, VLPET) and large LIF (LLIF) monochromators were used, as appropriate. Probe for EPMA software (Probe Software, Inc.) was used for quantitative analysis, which permitted the use of multi-point backgrounds (Allaz et al., 2019), multiple spectrometer count integration (P, Ti, Zr, Cr, S, V, Cd), and correction for time dependent effects such as element migration or surface contamination. Ti counts were corrected for PET diffraction effects near Ti Kα using a Ti-free synthetic SiO_2 glass as a blank. V counts were corrected for interference with Ti Kβ. Detection limits are reported in **Table 1**.

SEM-EBSD

Prior to electron backscatter diffraction (EBSD) analysis, mechanically polished thin sections were weighted with a halved brass rod and chemically polished for three hours in a non-crystallizing colloidal silica suspension on a Buehler Vibromet2 vibratory polisher (SYTON methods of Fynn & Powell, 1979).

Samples were rinsed in water and ethanol before drying overnight in a desiccator. A thin (3 to 10 nm) coat of carbon was applied to minimize charging.

The SEM was operated under high vacuum at 20 kV with a 15 nA beam current at working distances of 24–27 mm; samples were tilted at 70° towards the camera for EBSD analysis. Crystallographic orientation maps were collected using an Oxford Instruments NordlysMax^3 EBSD detector at Bowdoin College. Step size ranged from 8 to 25 μm, depending on the size of the analyzed grain. EBSD data were acquired with AZtec 3.2 (SP1) and post-processed with Channel5.12 software. Acquisition settings were 2 x 2 binning, gain = 7, Hough resolution = 90, 7 bands. Lattice parameters for the kyanite match unit were from Comodi et al. (1997) and mean angular deviations across all analyzed grains were <1°. Because post-processing can affect the integrity of the dataset (see discussion in Brewer & Michael, 2010), data were minimally processed with the intent of removing aberrant or unindexed points. Data were post-processed by interpolating unindexed pixels using the 6-nearest neighbors routine in Channel5. Non-systematic misindexed points (wild spikes) were removed. Because of the concern that post-processing might yield spurious results, we compared processed data with raw data; no obvious differences were observed, indicating minimal impact from post-processing.

RESULTS

Cathodoluminescence

The intensity and pattern of CL textures vary both within and among samples from a given locality (**Fig. 2**). We classify CL textures in kyanite into five categories: oscillatory, geometric, planar, patchy, and sector. Oscillatory zoning is a common texture in the analyzed kyanite (**Fig. 2a, g**); the absolute intensity and contrast within an oscillatory zoned domain varies widely, both within and among samples. Triangular or parallelogram forms are categorized as geometric (**Fig. 2c**). Planar domains are elongate and commonly oriented parallel to the long axis of the grain (**Fig. 2h**). Patchy domains exhibit a

range of internal features (**Fig. 2a, b, e, f, g, i**); some CL-dark patches are homogeneous (**Fig. 2a**), whereas others are mottled (**Fig. 2a**). Sector zones differ in CL intensity across a boundary forming wedge-shaped features; other textures (e.g., oscillatory zoning) remain traceable across the sector boundary (e.g., **Fig. 1a, 2d**).

Many kyanite grains exhibit more than one texture, and cross-cutting relationships permit reconstruction of the relative chronology of kyanite-forming or kyanite-modifying events. For example, many matrix-hosted kyanite grains have a discontinuous CL-bright rim that truncates the interior texture (e.g., **Figs. 2c, d, f–i; 3a; 4a; 5c**). Although this sequence of CL domains is common, it can be absent in grains from the same petrographic context or even in adjacent grains. In some grains, a CL-dark patch is truncated by an oscillatory zone or geometric texture (**Fig. 2b–g, i**).

EPMA Maps and Point Analyses

Trace element concentration maps show some variation in Fe and Mg and significant variation in P as measured by the integrated signal acquired for P (sum P) from three spectrometers (**Figs. 3–6**). Variations in all three elements negatively correlate with observed variation in CL intensity. Here we provide details on representative grains.

Northern Appalachians – Goshen Dome – G12B4 Kyanite 3

A kyanite porphyroblast from the Goshen Dome locality (**Fig. 3a-d**) is sector zoned in the interior; a thin CL-bright feature marks the end of the sector domain and the transition into an oscillatory zoned domain. The sector boundaries correspond to a sharp step-like function in P concentration (**Fig. 3c**), with higher P concentrations in the CL-dark sector. A small, relatively CL-dark patchy domain in the upper right-hand corner of the CL image also correlates with higher concentrations of P. Broadly similar patterns are apparent in the Fe and Mg maps; however, the relative change in concentration is smaller

329 than measured for P and the upper right corner feature with high-P is not evident in Fe or Mg maps.
330 Although higher concentrations of P correlate with low CL emission, not all CL-dark domains correlate
331 with high-P. For example, P concentrations are highest in the CL-dark sector; yet, the CL-dark portion of
332 the adjacent oscillatory zoned domain (white arrow, **Fig. 3a**) contains lower concentrations of P (and Fe,
333 Mg) than the sector domain. The CL-bright portion of the oscillatory zoned domain contains low
334 concentrations of P (and Fe, Mg) and subtle variations in trace element concentrations correlate with
335 variations in CL intensity.
336
337 *Rhodope – Xanthi – 57081X Kyanite 13*
338 A kyanite porphyroblast from the Xanthi locality of the Rhodope (**Fig. 3e-h**) has multiple
339 oscillatory zoned domains with different ranges of CL intensity. The central portion of the grain is CL-
340 bright and correlates with low concentrations of all measured trace elements (Fe, P, Mg). This domain is
341 surrounded by oscillatory zoned CL-dark(er) domains that correlate with high P concentrations; Fe is
342 weakly elevated, and there is no measured variation in Mg concentration. The lower right portion of the
343 grain is CL-dark with high P concentrations; no variation in Fe or Mg is observed. CL-dark does not
344 always correlate with high concentrations of P (or Fe, Mg). The CL-dark domain in the lower left does not
345 correlate with high or low concentrations of any measured trace elements.
346
347 *Northern Appalachians – Goshen Dome – G12B4 Kyanite 2*
348 A second kyanite porphyroblast from the Goshen Dome locality (**Fig. 4 a–d**) exhibits a patchy
349 zoned core surrounded by sector zoned domains and a CL-bright rim. The darkest CL domains within
350 the patchy core negatively correlate with high P concentrations, and Fe and Mg concentrations are
351 similarly high. Outside the core, the grain is sector zoned, as evident in CL images and trace element
352 maps, and shown schematically in **Fig. 4e**. Although all three trace element maps negatively correlate

with CL intensity, the variation in CL intensity in the core is best predicted by P concentrations: very low intensity CL corresponds precisely with the highest concentrations of P mapped within this grain. The CL-bright rim is very low in P, with moderate Fe + Mg concentrations. A blue halo surrounding monazite included in kyanite is the product of α-decay induced radiation damage (Rezvukhina et al., 2019). Quantitative point analyses collected from nine domains within this grain (**Fig. 4f**; locations of analysis locations are marked in **Fig. 4a**) are consistent with the trends observed in the compositional maps. The CL-dark domains contain 4 to 10 times higher concentrations of P (181–252 ppm) as compared with the CL-bright domains (20–34 ppm P). Similar trends are also evident in Fe and Mg (1580–1745 ppm vs. 1087–1371 ppm Fe; 126–181 ppm vs. 24–94 ppm Mg).

Additional trace element data were collected along two linear transects within this grain. Transect A (**Fig. 4g**) shows an increase in Cr near where the transect crosses into the CL-bright rim, as seen by correlation with the signal intensities extracted for each channel (lower panel in **Fig. 4g**). Ti concentrations vary along this transect, but do not correlate with changes in CL intensity. Transect B (**Fig. 4h**) crosses a sector boundary; whereas Cr does not vary with CL intensity, Ti concentrations are higher in the CL-dark sector, and lower in the CL-bright sector. Zr is essentially zero in all analyses. The CL signal intensities for Transect B vary widely, consistent with the patchy zoning in both sectors, and decrease by more than 50% at the sector boundary.

Northern Appalachians – Goshen Dome – G12B4 Kyanite 1

An elongate kyanite porphyroblast from the Goshen Dome (**Fig. 5**) exhibits undulatory extinction and a set of parallel kink bands. CL imaging reveals four textural domains. Domain 1 is located in the core of the grain and is characterized by planar variations in CL intensity; a boundary along the midline of the grain separates lower CL intensity kyanite on the bottom from higher CL intensity on the top. On the right end of the porphyroblast, the planar texture is truncated by CL-dark concentric zoning oriented

parallel to the short axis of the grain (domain 2). Domain 2 is truncated by a sharp, discontinuous CL-bright domain (3) parallel to the long axis of the grain that measures less than 100 μm thick and disappears at the tips. Along the top of the grain, parallel to the long axis, domain 3 is rimmed by domain 4, which is lower intensity CL with a planar texture.

Trace element maps reveal higher concentrations of both P and Fe in the dark portion of domain 1 (**Fig. 5d-e**); minor variations in CL are better predicted by P than Fe. None of the variation in CL observed in domains 2–4 are distinguishable in either P or Fe. Quantitative point data were collected along two transects (**Fig. 5f-g**) and CL signal intensity data were extracted along these transects (lower panels of **Fig. 5f-g**). Concentrations of Ti and Cr gradually decrease along the transect until reaching domain 3, where Cr sharply increases (200 ppm to nearly 500 ppm). Ti increases, but does not exceed the highest values measured from domain 1. Along transect 2, Cr drops from ~275 to 125 ppm, approximately coincident with the boundary of domain 2. Cr drops again from 250 ppm to below zero in the outermost portion of domain 2 (**Fig. 5g**; see also **Table A1, Supplementary Materials**). Ti concentrations broadly mimic Cr; Zr concentrations hover around zero until the outermost concentric zone, where they increase to 20 ppm.

Rhodope – Xanthi – 57081A (Kyanite 1, 3) and W17-001C2a (Kyanite 2, 6)

Trace element data were collected from three matrix kyanite and one garnet-hosted kyanite from the Xanthi locality (**Fig. 6**). The measured concentrations of Cd, Ge, S, Mn are at or below the lower detection limit, regardless of petrographic context or CL intensity (**Table A4**; **Supplementary Materials**). The CL-bright domains in matrix kyanite porphyroblasts contain up to five times more Cr than the CL-dark domains (**Fig. 6e**). Ti and P concentrations are nearly equivalent across all CL domains in matrix kyanite; the CL-dark portion of Ky 2 is slightly elevated in P. Fe and Mg concentrations within CL-bright domains vary among and within matrix grains. CL-dark domains have slightly lower concentrations of

Mg and Fe, except Ky 2, which has higher Fe concentrations in the CL-dark domain. Notably, the CL-dark domain in Ky 2 is texturally similar to garnet-hosted Ky 6.

Within the garnet-hosted kyanite (Ky 6), the CL-dark domain is significantly higher in P than all other domains—it is an order of magnitude higher in P than the CL-bright rim and it has triple the concentration of P of the matrix grains. As with the matrix grains, CL-dark domains contain less Fe and Cr than the CL-bright domains. The Cr concentrations are higher in the garnet-hosted kyanite than the matrix-hosted kyanite, regardless of CL intensity. Overall, Mg and Ti concentrations are similar to those measured in matrix grains.

EBSD

Kokchetav

A twinned kyanite porphyroblast from the Kokchetav whiteschist analyzed by EBSD exhibits a CL-dark domain surrounded by geometric domain that is truncated by a concentrically zoned CL-bright domain (**Fig. 7a**). In the upper-left portion of the grain, a patchy domain is truncated by a more homogeneous, low-intensity CL domain. The top right and lower right portions of the grain reveal steep gradients in crystallographic orientation, and the crystallographic orientation changes sharply along a kyanite twin. The crystallographic orientation gradually changes along the length of the grain, broadly parallel to the long axis; this gradual gradient extends across all domains (**Fig. 7b**), including patchy and CL-dark domains. A misorientation map shows that the gradual gradient in crystal orientation corresponds to 40° of misorientation (**Fig. 7c**). A subset of orientation data from this grain sampled from the lower right portion of the crystal shows that the crystal axes and the poles to the crystal planes cluster in the <010> direction and are dispersed in {100} and {001}. Great circles drawn 90° from the centroid of <010> contain nearly all the poles to the planes (**Fig. 7d**). Many grains also exhibit kink bands that reflect rotation of 10-50° about <010>. All EBSD findings are consistent with those reported from this sample by

Beane & Field (2007). Neither gradual nor sharp changes in crystal orientation correlate with variations in CL intensity or the boundaries of CL domains.

Rhodope

Kyanite porphyroblasts from the Rhodope Metamorphic Complex exhibit undulations in crystallographic orientation (**Fig. 8**). As with the Kokchetav sample, orientation data are clustered in the <010> direction and dispersed in {100} and {001}. A great circle that contains most – but not all – poles to the {100} and {001} planes is oriented 90° from <010>. Similarly, many grains exhibit kink bands that reflect rotation of 10–50° about <010>.

Northern Appalachians

Orientation data from kyanite porphyroblasts of the Cobble Mountain Formation (Goshen Dome locality) are clustered with minor smearing about <010> and dispersed in {100} and {001} (**Fig. 9a-h**). The poles to the planes of {100} and {001} fall along a great circle that is oriented 90° from <010>. Poles to [100] fall close to the same great circle but are not directly coincident. The dispersion of [100] and [001] can be partially explained by rotation about <010> with glide (100)[001], but because of the offset of [100] from the great circle, a tilt + twist boundary may better explain the observed trends. A series of kink bands are oriented at 75 to 80° from the long axis of the grain. Although most kink bands extend across the grain, some extend only partially across the grain. The orientation data show undulatory extinction perpendicular to the long axis of the grain with a 15° misorientation; individual undulations are <10° and range from steep to gradual along the length of the grain.

The amphibolite-facies rocks of the Northern Appalachians (P-84, P-1156, P-1168) show more varied microstructures in kyanite. These kyanite contain kink bands and undulatory extinction, but generally exhibit a lower abundance of kinking and lower amplitude undulations than in kyanite from

the (U)H*P* rocks from the Goshen Dome, Kokchetav, or Rhodope localities. Kyanite from P-84 (**Fig. 9i-l**) exhibits clustering of <010> and clustering of {100} and {001}. The data show minor dispersion in {001} along a great circle 90° to <010>; a subset of {100} is dispersed along the same great circle, with significant smearing above the great circle. In sample P-1156, the microstructures show some clustering about <010>, but with significant smearing (see **Supplemental Materials**). The data are dispersed in {100} and {001}, but do not conform to a single great circle and instead show significant smearing. Notably, the amplitude of undulatory extinction in the amphibolite-facies samples is <10° compared to 10–50° in the higher-pressure samples.

DISCUSSION

Significance of variations in crystallographic orientation

Previous studies suggested that sharp boundaries in crystallographic orientation might explain the variation in CL intensity and color observed (Schertl et al., 2004) or that crystal orientation may explain some of the variation that cannot be ascribed to variations in trace element concentrations (Götze et al., 2013; Kendrick & Indares, 2018). To evaluate these hypotheses, we analyzed samples that exhibit gradual and sharp variations in crystal orientation that are attributed to a range of mechanisms, including twinning, undulatory extinction, and kink banding. Our data show that none of these changes in absolute crystallographic orientation (from 2 to 50°) correspond with changes in CL intensity in any of the measured samples. For example, G12B4_ky7 consists of four CL domains (**Fig. 5**), but none of the observed variations in CL intensity correlate with changes in crystallographic orientation. Similarly, our analysis of kyanite from Kokchetav (**Fig. 7**) reveals that neither the twin boundary (~90° of misorientation) nor the smooth misorientation gradient (nearly 50° from top to bottom) correlate with any variations in CL intensity. These observations are consistent with Rezuvkhina et al. (2019) and expand the range over which changes in orientation are demonstrated to not correlate with changes in CL from >10°

473 to 90° of misorientation. These data also show that twinned kyanite is not expected to produce a variation
474 in CL intensity or color.

475 Crystallographic orientation data can provide insights about the mechanisms and relative timing
476 of deformation. Our results are consistent with results from natural rocks (Lenze et al., 2005; Beane &
477 Field, 2007) and experimental work (Raleigh, 1965) that showed that both kink banding and undulatory
478 extinction in kyanite are accommodated by rotation about <010> in the (100)[001] slip system. In naturally
479 deformed rocks exhumed from UH*P* conditions, kyanite kink bands form in response to inhomogeneous
480 internal stress that results from transformations of major constituent phases (Lenze et al., 2005).
481 Increasing strain correlates with a decrease in kink-band width and increased rotation of (100) about
482 <010> within the kinks (Boland, et al., 1977). Matrix kyanite from UH*P* conditions are consistent with
483 these findings, and tightly-spaced kink bands with a high degree of rotation of (100) abut <010> are
484 particularly abundant in Rhodope samples. Kyanite porphyroblasts devoid of deformation are found
485 either as inclusions in garnet porphyroblasts or as tiny grains that form part of a larger aggregate in the
486 matrix. Therefore, we interpret that the major phase of kink banding occurred post-garnet growth, likely
487 during exhumation, concurrent with phase transformations; intact garnet porphyroblasts shielded
488 included kyanite from deformation. Matrix kyanite grains that lack microstructural evidence of
489 deformation likely formed post-deformation, though the mechanism for (re)crystallization remains
490 unknown.

491 Given that undulatory extinction is preserved in cases where the lattice does not recover (e.g.,
492 low temperatures inhibiting dislocation climb, insufficient strain following the original deformation;
493 Blenkinsop, 2002), and that undulatory extinction and kink banding occur along the same slip systems in
494 kyanite, we suggest that differences in the amplitude of undulations may correspond to the conditions at
495 which the microstructure formed. For example, the magnitude of misorientation measured from
496 undulating domains from the lower grade assemblages is lower than that measured in the (U)H*P* rocks,

consistent with lower overall strain. The lower grade rocks also exhibit greater variability in the orientation of microstructures, consistent with more heterogeneous strain. A systematic evaluation of these data may prove fruitful for identifying differences in strain along the *P*-T path.

Correlations among trace element geochemistry and CL intensity

CL-dark domains: Fe and P

As suggested by previous studies (Götze et al., 2011; 2013), CL-dark domains in kyanite analyzed in this study often contain higher Fe concentrations than adjacent CL-bright domains (e.g., **Figs. 4b, 4f, 6c**), consistent with Fe quenching CL emission. However, we note that our measured concentrations are lower than those typically thought to quench CL (Müller et al., 2016). Additionally, several examples contradict this pattern. Three kyanite grains from Rhodope (**Fig. 6**) yield higher Fe concentrations in the CL-bright domains than in the adjacent CL-dark domains. Other mapped kyanite grains reveal slight differences in Fe concentration between CL-bright and CL-dark domains (**Figs. 3, 5**). Still, we note that CL intensity correlates quite well with P concentrations in some domains. Where a correlation between CL intensity and P concentration is observed, Fe does not show a commensurate change in concentration. Instead, the CL intensity is the absolute darkest in the image and there is a marginal increase in Mg concentration (e.g., the brightest domains in **Fig. 4c**).

The spatial context of CL-dark domains with locally high concentrations of P (+ Mg) may be a critical factor in determining their potential significance. In the analyzed grains, domains with locally high concentrations of P (+ Mg) are located in the grain interiors, never along grain margins even in domains with relatively low CL emission. This spatial restriction suggests that enrichment in P (+ Mg) may be related to metamorphism at prograde (or peak) conditions. Experimental work suggests that there is good reason to examine P (+ Mg)-rich domains, particularly within interior domains in kyanite, as Konzett (2016) reported unexpectedly high concentrations of P (0.17–0.20 wt% P_2O_5) and Mg (0.20–

0.56 wt.% MgO) in kyanite from mafic eclogites and melts. Konzett (2016) interpreted this resulted from coupled substitution into the crystal structure via:

$$^{[4]}Si^{4+} + {}^{[6]}Al^{3+} = {}^{[4]}P^{5+} + {}^{[6]}Mg^{2+}$$

and suggested that high-P (+ Mg) domains within kyanite in metapelites may also record UH*P* conditions. Results from the Goshen Dome sample are consistent with this proposed mechanism; CL-dark domains with high concentrations of P (**Fig. 4**) have a near 1:1 stoichiometric relationship between Mg and P whereas other analyzed domains yield highly variable Mg:P (7:1 to 0.7:1). The CL-dark domain within the garnet-hosted kyanite from Rhodope (**Fig. 6d-e**) yields a Mg:P of 0.45:1 and the other kyanite domains range from 0.25:1 to 4:1.

Results from (U)H*P* metapelites in our study provide an initial dataset to test the idea that elevated P concentrations in kyanite may reflect extreme pressures. The CL-dark domain within a kyanite porphyroblast from Rhodope (**Fig. 6d**) is notably elevated in P (+ Mg), and this kyanite is included within garnet that itself contains indicators of UH*P* metamorphism (e.g., crystallographically oriented inclusions—Keller & Ague, 2019; high intrinsic P_2O_5—Ague & Axler, 2016; Peterman et al., 2016b). Domains enriched in P (+Mg) are not common in matrix kyanite, suggesting that kyanite armored by garnet may preserve earlier components of the *P-T* path that are commonly overprinted or recrystallized in the matrix. Large kyanite porphyroblasts from the Goshen Dome (U)H*P* locality preserve high-P + Mg domains (**Fig. 3c, 4c**) with a 1:1 stoichiometric relationship in the central portion of the grains, and not along the margins, which is texturally consistent with an earlier growth history, perhaps at high-*P*. Unfortunately, very few P measurements have been made in kyanite, particularly in metapelitic assemblages. Apatite and monazite are key hosts of P in metapelitic rocks (e.g, Spear & Pyle, 2002; Kelsey et al., 2008; Spear & Pyle, 2010), but little experimental work has been published that explores other reservoirs for P in metapelitic bulk compositions. Partial dissolution of monazite or apatite could provide a source of P; however, given the abundance of both monazite and apatite throughout the sample

(including in kyanite), we might expect P-enriched domains to be more widespread and not restricted to the interior domains of kyanite. The dataset is not yet robust enough to fully evaluate the significance of high P (+ Mg) concentrations in kyanite, but these findings are curious.

CL-bright domains: Cr and Ti

Trace element analyses (**Figs. 4-6**) show that high concentrations of Cr often correspond with CL-bright domains. The converse, however, is not always true; CL-bright domains in **Fig. 6c** yield similar Cr concentrations as the CL-dark domains and variations in CL intensity along transect B (Fig. 4h) do not correspond to a change in Cr concentration. These findings underscore that interpreting the significance of CL textures requires an understanding of the textural context of the kyanite domain. Cr-rich domains can be inherited from Cr-rich minerals (e.g., micas) that were overprinted by kyanite during metamorphism (Yang & Rivers, 2001). The finely laminated CL-bright, Cr-rich domains with kyanite from the Rhodope (**Fig. 6b**) likely reflect the texture and geochemistry of overprinted white mica. Similarly, variations in CL intensity and the angular relationships among internal domains observed in the largest kyanite in **Fig. 2i** are likely attributed to inherited textures from staurolite (photomicrographs of thin section included in **Supplemental Materials**).

In contrast, CL-bright domains enriched in Cr located near the margins of kyanite are unlikely to be inherited textures, and more likely result from melting reactions. A prime example is the kyanite featured in **Fig. 5.** The CL-bright domain (earlier described as domain 3) contains >300 ppm Cr, exhibits oscillatory zoning that is concentric with the core of the grain, and truncates portions of the inner domain. This grain is now surrounded by chlorite + quartz + phlogopite, and the margins indicate partial resorption during recrystallization, but the event that formed the CL-bright domains predates the retrograde assemblage. Similar CL-bright kyanite domains have previously been interpreted as a product of metasomatism or a reaction with melt (Kendrick & Indares, 2018). Because garnet can carry significant

569 Cr concentrations (Martin, 2009; Yang & Rivers, 2001), partial breakdown or resorption of garnet may
570 lead to enrichment in Cr in the fluid or melt through the reaction

571 garnet + K-feldspar + melt → biotite + plagioclase + kyanite + quartz

572 The resorbed garnet rims in this restitic schist and the migmatitic rocks adjacent to the sample are
573 consistent with melt extraction, and suggest that this reaction is plausible for the production of the CL-
574 bright, Cr-rich domains. An alternative reaction

575 muscovite + quartz → melt + K-feldspar + kyanite

576 may also release Cr in muscovite to the melt, which then becomes available to other phases (e.g., garnet;
577 Kohn et al., 1997), but the low abundance of K-feldspar in these rocks favors the first reaction. In either
578 case, we interpret that the CL-bright domains along kyanite margins are not inherited from the
579 overprinted mineral but instead reflect melt-related growth. That the phlogopite matrix is now partially
580 replaced by chlorite underscores the potential durability of the record preserved within kyanite—as well
581 as the difficulty in extracting this history in samples where the matrix is fully recrystallized. Interestingly,
582 the core of this grain exhibits a steady decrease in Cr concentration while maintaining a broadly uniform
583 CL intensity in the red wavelengths, as shown in **Fig. 5f.** This finding further highlights the challenge of
584 using CL as a proxy for single element variation in kyanite.

585 Previous studies have shown that high-Ti concentrations in kyanite correspond with blue CL
586 emission (Müller et al., 2016) and, as with Ti-in-quartz thermometry (Wark & Watson, 2006), suggest a
587 potential for single element thermometry within kyanite as guided by CL images. Transect B in **Fig. 4h**
588 shows a good correlation between CL intensity and Ti concentration, but this trend is inconsistent among
589 samples. Instead, the full dataset shows increasing and decreasing Ti concentrations with both uniform
590 and decreasing CL intensity. This inconsistency shows that panchromatic and color CL images cannot be
591 reliably used to predict Ti concentrations in kyanite; instead, a CL spectral analyzer (monochromator)
592 may be more useful in evaluating correlations between Ti and CL emission.

The relationships between trace element geochemistry and CL intensity demonstrate that CL images can provide a useful guide for locating domains for trace element analysis. However, our data show that CL intensity alone cannot be used to locate domains characterized by enrichment in a single trace element, as evidenced by the non-systematic correlations between CL intensity and Cr, Ti, Fe, or P (**Figs. 4-6)**. Furthermore, some kyanite grains exhibit no variation in measured trace elements within the sensitivity of the EPMA analyses, despite textures observed in CL. Even in the same sample, kyanite with the same CL intensity and color yields different trace element concentrations (**Fig. 4 & 5; Fig. 6c-e**).

Kyanite from the Xanthi locality within the Rhodope Metamorphic Complex (**Fig. 6**) illustrate the importance of examining correlations among petrographic context, CL textures and intensity, and geochemistry—and the potential significance of local equilibria on the growth or resorption of kyanite. Both Ky 1 and Ky 3 are matrix grains from the same sample; they both feature dark CL domains with little internal texture and yield comparable trace element concentrations. Based on similarities in CL, composition, and context, these domains are interpreted to have formed during the same event. In a nearby sample (W17-001C2a), Ky 6 is included within a 2-cm diameter garnet porphyroblast and exhibits CL-dark patches and oscillatory zoned domains with high concentrations of P and Cr. Ky 2, located in the matrix of the same sample, also has CL-dark domains, but this domain features a mottled zoning texture, contains lower concentrations of nearly all trace elements, and is riddled with inclusions, some of which are also rimmed by CL-bright domains. These differences in texture and composition suggest that the CL-dark portion of Ky 2 either formed during a different reaction from Ky 6 or was chemically modified at a later stage. Because several elements affect CL intensity in kyanite, the presence of a CL-bright or CL-dark domain cannot be correlated to one specific trace element, even in the same sample. Therefore, interpreting the significance of CL domains requires consideration of the distribution of textures and CL intensities with respect to the petrographic context, similar to "zirconology" (e.g., Hanchar & Hoskin, 2003; Rubatto, 2002).

CONCLUSIONS

The data presented support the following conclusions, which have implications for future studies of kyanite-bearing lithologies.

(1) Absolute orientation, the occurrence of kyanite twins, and relative misorientation within a kyanite grain do not correlate with CL intensity or color.

(2) The amplitude of undulations and the tightness of clustering about <010> correlate with the magnitude and homogeneity of strain; systematic evaluation of kyanite with known strain histories would provide useful insight into this observation.

(3) Kyanite porphyroblasts preserve cross-cutting textural relationships, highlighting the persistence of trace element zoning and CL intensity through multiple events. Some textures are inherited from precursor phases, whereas others formed during melting events. In other cases, progressive metamorphism has eliminated the possibility of directly linking domains to events or paragenetic minerals.

(4) CL color broadly correlates with Cr and Ti, but Fe, P, and Mg concentrations can significantly impact color and intensity. Depending on the concentration, Fe can activate or quench CL emission; P and Mg appear always to quench CL emission.

(5) P concentrations may be particularly important in UH*P* rocks, as kyanite can serve as a reservoir of P at UH*P*; using CL to identify potential domains for investigation may be a useful approach. Because multiple elements affect CL emission, panchromatic and RGB filtered CL images alone are not a reliable proxy for trace element concentrations. Instead, these images should be used as a guide for trace element analysis.

ACKNOWLEDGEMENTS

641 The authors thank Richard White for editorial handling, and Frank Spear and Chris Gerbi for
642 helpful reviews. This work was supported in part by NSF EAR-1650054 to Peterman, and by Bowdoin
643 College Research Funds. The SEM facility is supported by NSF MRI-1530963 to Peterman and Beane, and
644 by Bowdoin College. The UltraChron development project was supported by NSF EAR-0004077 and NSF
645 EAR-0549639 to M.L. Williams and M.J. Jercinovic at the University of Massachusetts, and collaboratively
646 by Cameca. C. de Wet was supported by a Surdna Foundation Research Fellowship through Bowdoin
647 College. Peterman thanks M. Calentti, S. Crawford, and T. Peterson for analytical assistance.

REFERENCES

Ague, J.J., & Axler, J.A. (2016) Interface coupled dissolution-reprecipitatoin in garnet from subducted granulites and ultrahigh-pressure rocks revealed by phosphorous, sodium, and titanium zonation. *American Mineralogist, 101*: 1696–1699. http://dx.doi.org/10.2138/am-2016-5707

Ague, J. J., & Eckert, J. O. (2012). Precipitation of rutile and ilmenite needles in garnet: Implications for extreme metamorphic conditions in the Acadian orogen, U.S.A. *American Mineralogist, 97*(5): 840-855. doi:10.2138/am.2012.4015

Ague, J. J., Eckert Jr, J. O., Chu, X., Baxter, E. F., & Chamberlain, C. P. (2013). Discovery of ultrahigh-temperature metamorphism in the Acadian orogen, Connecticut, USA. *Geology, 41*(2): 271-274. doi:10.1130/G33752.1

Albee, A.L. & Chodos, A.A. (1969) Minor element content of coexistent Al_2SiO_5 polymorphs. *American Journal of Science.* 267(3): 310-316. doi: 10.2475/ajs.267.3.310

Allaz, J.M., Williams, M.L., Jercinovic, M.J., Goemann, K., & Donovan, J. (2019). Multipoint background analysis: Gaining precision and accuracy in microprobe trace element analysis. *Microscopy & Microanalysis*, 25(1): 30-46. https://doi.org/10.1017/S1431927618015660

Armstrong, T. R., Tracy, R. J., & Hames, W. E. (1992). Contrasting styles of Taconian, eastern Acadian and western Acadian metamorphism, central and western New England. *Journal of Metamorphic Geology,* 10(3): 415-426. doi:10.1111/j.1525-1314.1992.tb00093.x

Ashley, K. T., Webb, L. E., Spear, F. S., & Thomas, J. B. (2013). P-T-D histories from quartz: A case study of the application of the TitaniQ thermobarometer to progressive fabric development in metapelites. *Geochemistry, Geophysics, Geosystems, 14*(9): 3821-3843. doi:10.1002/ggge.20237

Barrow G. (1893) On an intrusion of muscovite-biotite gneiss in the south-eastern Highlands of Scotland, and its accompanying metamorphism. *Quarterly Journal of the Geological Society of London*. 49: 330–358.

Beane, R. J., & Field, C. K. (2007). Kyanite deformation in whiteschist of the ultrahigh-pressure metamorphic Kokchetav massif, Kazakhstan. *Journal of Metamorphic Geology, 25*(2): 117-128. doi:10.1111/j.1525-1314.2007.00692.x

Blenkinsop, T. (2002). Deformation Microstructures and Mechanisms in Minerals and Rocks. Kluwer Academic Publishers, New York.

Boggs, S. Jr. & Krinsley, D. (2006) Application of Cathodoluminescence Imaging to the Study of Sedimentary Rocks. Cambridge University Press, 176 pp.

Boland, J.N., Hobbs, B.E. & McLaren, A.C. (1977). The Defect Structure in Natural and Experimentally Deformed Kyanite. *Phys. Stat. Sol. A.* 39: 631-641.

Brewer, L.N., & Michael, J.R. (2010) Risks of "Cleaning" Electron Backscatter Diffraction Data. Microscopy-Today. 10-15. doi: 10.1017/S1551929510000040

Chadwick, K. M. and Rossman, G. R. (2009) *Orange kyanite from Tanzania.* Gems and Gemology, 45(2): 146-147.

Cheney, J.T., Spear, F.S., & Kirk-Lawlor, N. (2006) The mysterious machinations of muscovite and monazite during metamorphism or How the CVS (Connecticut Valley synclinorium) survived PMS (post-metamorphic-stretching). Geological Society of America Abstracts with Programs, 38, 49, https://gsa.confex.com/ gsa/2006AM/finalprogram/abstract_113956.htm.

Chinner, G. A., Smith, J. W., Knowles, C. R. (1969) Transition metal contents of Al_2SiO_5 polymorphs. *American Journal of Science*, 267A: 96-113.

Clark, S. P., Robertson, E. C., Birch, F. (1957) Experimental determination of kyanite-sillimanite equilibrium relations at high temperatures and pressure. *American Journal of Science*, 255: 628-640.

Comodi, P., Zanazzi, P. F., Poli, S., & Schmidt, M. W. (1997). High-pressure behavior of kyanite: Compressibility and structural deformations. *American Mineralogist, 82*(5): 452-459. doi:10.2138/am-1997-5-602

Corfu, F., Hanchar, J. M., Hoskin, P. W. O., & Kinny, P. (2003). Atlas of zircon textures. *Reviews in Mineralogy and Geochemistry, 53*(1): 469-500. doi:10.2113/0530469

Deer, WA, Howie, RA, and Zussman, J (1997): Rock Forming Minerals: Orthosilicates, 2nd edition, Vol. 1A. Geological Society, Bath: pp. 919.

Dietsch, C. (1989). The Waterbury dome, west-central Connecticut: A triple window exposing deeply deformed, multiple tectonic units. *American Journal of Science,* 289(9): 1070-1097.

Dragovic, B., Gatewood, M.P., Baxter, E.F., & Stowell, H.H. (2018). Fluid production rate during the regional metamorphism of a pelitic schist. *Contributions to Mineralogy and Petrology. 173:* 96.

Faye, G.H., & Nickel, E.H. (1969). On the Origin of Colour and Pleochroism of Kyanite. *The Canadian Mineralogist, 10:* 35-46.

Ferry, J. M., & Spear, F. S. (1978). Experimental calibration of the partitioning of Fe and Mg between biotite and garnet. *Contributions to Mineralogy and Petrology, 66*(2): 113-117. doi:10.1007/BF00372150

Fynn, G.W. & Powell W. (1979). The Cutting and Polishing of Electro-optic Materials. Adam Hilger, London, 1979.

Gaft, M., & Panczer, G. (2013). Laser-induced time-resolved luminescence spectroscopy of minerals: A powerful tool for studying the nature of emission centres. *Mineralogy and Petrology,* 107(3): 363-372. doi:10.1007/s00710-013-0293-3

Gatewood, M. P., Dragovic, B., Stowell, H. H., Baxter, E. F., Hirsch, D. M., & Bloom, R. (2015). Evaluating chemical equilibrium in metamorphic rocks using major element and Sm–Nd isotopic age zoning in garnet, Townshend Dam, Vermont, USA. *Chemical Geology*, 401: 151-168. doi:10.1016/j.chemgeo.2015.02.017

Ghent, E.D., 1976. Plagioclase-garnet-Al2SiO5 quartz: a potential geobarometer-geothermometer. American Mineralogist, 6l: 710-714

Götze, J., & Kempe, U. (2008). A comparison of optical microscope- and scanning electron microscope-based cathodoluminescence (CL) imaging and spectroscopy applied to geosciences. *Mineralogical Magazine, 72*(4): 909-924. doi:10.1180/minmag.2008.072.4.909

Götze, J., Plötze, M., & Habermann, D. (2001). Origin, spectral characteristics and practical applications of the cathodoluminescence (CL) of quartz – a review. *Mineralogy and Petrology, 71*(3): 225-250. doi:10.1007/s007100170040

Götze, J., Schertl, H-P., Neuser, R. D., Kempe, U. & Hanchar, J. M. (2013). Optical microscope-cathodoluminescence (OM–CL) imaging as a powerful tool to reveal internal textures of minerals. *Mineralogy and Petrology, 107*(3:, 373-392. doi:10.1007/s00710-012-0256-0

Grujic, D., Stipp, M., & Wooden, J. L. (2011). Thermometry of quartz mylonites: Importance of dynamic recrystallization on Ti-in-quartz reequilibration. *Geochemistry, Geophysics, Geosystems,* 12(6). doi:10.1029/2010GC003368

Habermann, D. (2002). Quantitative cathodoluminescence (CL) spectroscopy of minerals: Possibilities and limitations. *Mineralogy and Petrology,* 76(3): 247-259. doi:10.1007/s007100200044

Hames, W. E., Tracy, R. J., & Bodnar, R. J. (1989). Postmetamorphic unroofing history deduced from petrology, fluid inclusions, thermochronometry, and thermal modeling: An example from southwestern New England. *Geology*, 17(8): 727-730. doi:10.1130/0091-7613(1989)017<0727:PUHDFP>2.3.CO;2

Hanchar, J. M., & Miller, C. F. (1993). Zircon zonation patterns as revealed by cathodoluminescence and backscattered electron images: Implications for interpretation of complex crustal histories. *Chemical Geology,* 110(1-3): 1-13. doi:10.1016/0009-2541(93)90244-D

Hanchar, J.M. & Hoskin, P.W.O. (2003). Zircon. *Reviews in Mineralogy and Geochemistry*. 53(1): 500 pp.

Hatch, N.L. Jr., & Warren, C.R. (1981) Geologic map of the Goshen quadrangle, Franklin and Hampshire Counties, Massachusetts. U.S. Geological Survey Geologic Quadrangle Map GQ-1561, scale 1: 24,000, http://pubs.er.usgs.gov/ publication/gq1561.

Herz N., & Dutra, C.V. (1964) Geochemistry of some kyanites from Brazil. *American Mineralogist*, 49: 1290–1305.

Hibbard, J. P., Van Staal, C. R., & Rankin, D. W. (2007). A comparative analysis of pre-Silurian crustal building blocks of the northern and the southern Appalachian orogen. *American Journal of Science,* 307(1): 23-45. DOI 10.2475/01.2007.02]

Holdaway, M.J. (2000). Application of new experimental and garnet Margules data to the garnet-biotite geothermometer. *American Mineralogist.* 85 (7-8): 881–892. https://doi.org/10.2138/am-2000-0701

Horkley, L.K., Spear, F.S., Ruscitto, D.M., and Tailby, N.D. (2013). The secret life of kyanite. Geological Society of America, 48th Annual Meeting, paper no. 43-1.

Huang, R., & Audétat, A. (2012). The titanium-in-quartz (TitaniQ) thermobarometer: A critical examination and re-calibration. *Geochimica et Cosmochimica Acta*, 84: 75-89. doi:10.1016/j.gca.2012.01.009

Janák, M., Froitzheim, N., Georgiev, N., Nagel, T. J., & Sarov, S. (2011). P–T evolution of kyanite eclogite from the Pirin mountains (SW Bulgaria): Implications for the Rhodope UHP metamorphic complex. *Journal of Metamorphic Geology,* 29(3): 317-332. doi:10.1111/j.1525-1314.2010.00920.x

Karabinos, P., Samson, S. D., Hepburn, J. C., & Stoll, H. M. (1998). Taconian orogeny in the New England Appalachians: Collision between Laurentia and the Shelburne Falls Arc. *Geology, 26*(3): 215-218. doi:10.1130/0091-7613(1998)026<0215:TOITNE>2.3.CO;2

Karabinos, P., Macdonald, F.A., & Crowley, J.L. (2017) Bridging the gap between the foreland and hinterland I: Geochronology and plate tectonic geometry of Ordovician magmatism and terrane accretion on the Laurentian margin of New England. *American Journal of Science.* 317(5): 515-554. doi: 10.2475/05.2017.01

Keller, D. S., & Ague, J. J. (2019). Crystallographic and textural evidence for precipitation of rutile, ilmenite, corundum, and apatite lamellae from garnet. *American Mineralogist, 104*(7): 980-995. doi:10.2138/am-2019-6849

Keller, D.S., & Ague, J.J. (2020) Quartz, mica, and amphibole exsolution from majoritic garnet reveals ultra-deep sediment subduction, Appalachian orogen. *Science Advances, 6, 11, eaay5178.* DOI: 10.1126/sciadv.aay5178 (2020)

Kelsey, D.E, Clark, C., & Hand. M. (2008) Thermobarometric modelling of zircon and monazite growth in melt-bearing systems: examples using model metapelitic and metapsammitic granulites. *Journal of Metamorphic Geology, 26*(2): 199-212. https://doi.org/10.1111/j.1525-1314.2007.00757.x

Kendrick, J., & Indares, A. (2018). The reaction history of kyanite in high-P aluminous granulites. *Journal of Metamorphic Geology, 36*(2): 125-146. doi:10.1111/jmg.12286

Kidder, S., Avouac, J.-P., & Chan, Y.-C. (2013). Application of titanium-in-quartz thermobarometry to greenschist facies veins and recrystallized quartzites in the Hsüehshan range, Taiwan. *Solid Earth, 4*(1): 1-21. doi:10.5194/se-4-1-2013

Kirchenbaur, M., Pleuger, J., Jahn-Awe, S., Nagel, T.J., Froitzheim, N., Fonseca, R.O.C., & Münker, C. (2012). Timing of high-pressure metamorphic events in the Bulgarian Rhodopes from Lu–Hf garnet geochronology. *Contributions to Mineralogy and Petrology, 163*(5): 897-921. doi:10.1007/s00410-011-0705-5

Kohn, M. J., & Spear, F. S. (1990). Two new geobarometers for garnet amphibolites, with applications to southeastern Vermont. *American Mineralogist, 75*(1-2): 89-96.

Kohn, M.J., Spear, F.S., and Valley, J.W. (1997). Dehydration-melting and fluid recycling during metamorphism: Rangeley Formation, New Hampshire, USA. *Journal of Petrology*, *38*(9): 1255-1277.

Konzett, J. (2016). From phosphates to silicates and back: An experimental study on the transport and storage of phosphorus in eclogites during uplift and exhumation. *American Mineralogist, 101*(8): 1756-1768. doi:10.2138/am-2016-5521

Krenn, K., Bauer, C., Proyer, A., Klötzli, U., & Hoinkes, G. (2010). Tectonometamorphic evolution of the Rhodope orogen. Tectonics 29, TC4001.

Lanzirotti, A., & Hanson, G. N. (1995). U-Pb dating of major and accessory minerals formed during metamorphism and deformation of metapelites. *Geochimica Et Cosmochimica Acta, 59*(12): 2513-2526. doi:10.1016/0016-7037(95)00146-8

Law, R. D. (2014). Deformation thermometry based on quartz c-axis fabrics and recrystallization microstructures: A review. *Journal of Structural Geology, 66*: 129-161. doi:10.1016/j.jsg.2014.05.023

Lenze, A., Stöckhert, B., & Wirth, R. (2005). Grain scale deformation in ultra-high-pressure metamorphic rocks—an indicator of rapid phase transformation. *Earth and Planetary Science Letters, 229*(3): 217-230. doi:10.1016/j.epsl.2004.10.012

Liati, A. (2005). Identification of repeated alpine (ultra) high-pressure metamorphic events by U–Pb SHRIMP geochronology and REE geochemistry of zircon: The Rhodope zone of Northern Greece. *Contributions to Mineralogy and Petrology, 150*(6): 608-630. doi:10.1007/s00410-005-0038-3

Liati, A., Theye, T., Fanning, C. M., Gebauer, D., & Rayner, N. (2016). Multiple subduction cycles in the Alpine orogeny, as recorded in single zircon crystals (Rhodope zone, Greece). *Gondwana Research, 29*(1): 199-207. doi:10.1016/j.gr.2014.11.007

Macdonald, F., Ryan-Davis, J., Coish, R., Crowley, J., & Karabinos, P. (2014). A newly identified Gondwanan terrane in the northern Appalachian Mountains: Implications for the Taconic orogeny and closure of the Iapetus ocean. *Geology, 42*(6): 539.

Martin, A.J. (2009) Sub-millimeter heterogeneity of yttrium and chromium during growth of semi-pelitic garnet. *Journal of Petrology.* 50(9): 1717-1727. https://doi.org/10.1093/petrology/egp050

Menard, T., & Spear, F. S. (1994). Metamorphic P-T paths from calcic pelitic schists from the Strafford Dome, Vermont, USA. *Journal of Metamorphic Geology, 12*(6): 811-826. doi:10.1111/j.1525-1314.1994.tb00061.x

Mposkos, E., Kostopoulos, D., Perraki, M., Proyer, A., Kaindl, R., Hoinkes, G. (2001). The Greek Rhodope: A New UHPM Province, UHPM Workshop 2001 at Waseda University, 3P10: 218-222

Müller A., van den Kerhof A.M., & Broekmans M.A. (2012) Trace Element Content and Optical Cathodoluminescence of Kyanite. In: Broekmans M. (eds) Proceedings of the 10th International Congress for Applied Mineralogy (ICAM): 453-461. https://doi.org/10.1007/978-3-642-27682-8_54

Müller A., van den Kerhof A.M., Selbekk, R.S. & Broekmans M.A. (2016) Trace element composition and cathodoluminescence of kyanite and its petrogenetic implications. *Contributions to Mineralogy and Petrology.* 171: 70. doi:10.1007/s00410-016-1280-6

Miyashiro, A., 1949, The stability relation of kyanite, sillimanite, and andalusite, and the physical conditions of the metamorphic processes: Journal of the Geological Society of Japan, v. 55, p. 218–223, doi:10.5575/geosoc.55.218

Nachlas, W. O., Whitney, D. L., Teyssier, C., Bagley, B., & Mulch, A. (2014). Titanium concentration in quartz as a record of multiple deformation mechanisms in an extensional shear zone. *Geochemistry, Geophysics, Geosystems, 15*(4): 1374-1397. doi:10.1002/2013GC005200

Neiva, A. M. R. (1984). Chromium-bearing kyanite from Mozambique. *Mineralogical Magazine, 48*(4): 563-564.

Newton, R.C. & Haselton, H.T. (1981) Thermodynamics of the Garnet-Plagioclase-Al_2SiO_5-Quartz Geobarometer. In: Newton R.C., Navrotsky A., Wood B.J. (eds) Thermodynamics of Minerals and Melts. Advances in Physical Geochemistry, vol 1. Springer, New York, NY. https://doi.org/10.1007/978-1-4612-5871-1_7

Ostapenko, G.T., Gamarnik, M.Y., Gorogotskaya, L.I., Kuznetsov, G.V., Tarashchan, A.N., Timoshkova, L.P. (1987) Isomorphism of titanium substitution for silicon in quartz: experimental data. *Mineralogicheskii Zhurnal* 9: 30–40.

Ostapenko, G. T., Tarashchan, A. N., & Mitsyuk, B. M. (2007). Rutile-quartz geothermobarometer. *Geochemistry International, 45*(5): 506-508. doi:10.1134/S0016702907050084

Owens, B. E., & Dickerson, S. E. (2001). Kyanite color as a clue to contrasting protolith compositions for kyanite quartzites in the piedmont province of Virginia. *Southeastern Geology, 40*(4): 285-298.

Parkinson, C. D. (2000). Coesite inclusions and prograde compositional zonation of garnet in whiteschist of the HP-UHPM Kokchetav massif, Kazakhstan: A record of progressive UHP metamorphism. *Lithos, 52*(1): 215-233. doi:10.1016/S0024-4937(99)00092-4

Passchier C. W., & Trouw, R. A. J. (2005) Microtectonics. Springer-Verlag Berlin Heidelberg. 366 pp. ISBN 978-3-540-29359-0

Pearson, G. R. & Shaw, D. M. (1960) Trace elements in kyanite, sillimanite and andalusite. *American Mineralogist*, 45: 808-817.

Peterman, E. M., & Grove, M. (2010). Growth conditions of symplectic muscovite + quartz: Implications for quantifying retrograde metamorphism in exhumed magmatic arcs. *Geology, 38*(12): 1071-1074. doi:10.1130/G31449.1

Peterman, E.M., Burton, Z.F.M., Rubel, J.N., Snoeyenbos, D.R. and Kylander-Clark, A. (2014) Monazite petrochronology via LASS characterizes 30 Myr of episodic retrograde metamorphism in western Massachusetts. V43B-4886, AGU Fall Meeting, San Francisco. Dec. 15-19.

Peterman, E. M., Reddy, S. M., Saxey, D. W., Snoeyenbos, D. R., Rickard, W. D. A., Fougerouse, D., & Kylander-Clark, A. R. C. (2016a). Nanogeochronology of discordant zircon measured by atom probe microscopy of pb-enriched dislocation loops. *Science Advances, 2*(9): e1601318. doi:10.1126/sciadv.1601318

Peterman, E. M., Snoeyenbos, D. R., Jercinovic, M. J., & Kylander-Clark, A. (2016b). Dissolution-reprecipitation metasomatism and growth of zircon within phosphatic garnet in metapelites from western Massachusetts. *American Mineralogist, 101*(8): 1792-1806. doi:10.2138/am-2016-5524

Peterman, E. M., Reddy, S. M., Saxey, D. W., Fougerouse, D., Snoeyenbos, D. R., & Rickard, W. D. A. (2019). Nanoscale processes of trace element mobility in metamorphosed zircon. *Contributions to Mineralogy and Petrology, 174*(11): 1-29. doi:10.1007/s00410-019-1631-1

Pyle, J. M., Spear, F. S., Wark, D. A., Daniel, C. G., & Storm, L. C. (2005). Contributions to precision and accuracy of monazite microprobe ages. *American Mineralogist, 90*(4): 547-577. doi:10.2138/am.2005.1340

Raleigh, C.B. (1965) Glide mechanisms in experimentally deformed minerals. *Science* 150: 739–741.

Ramirez, B.R., Moecher, D., & Dietsch, C. (1996). Textural and chemical zoning constraints on interpretation of Acadian *P-T* conditions, southern Connecticut Valley zone, New England: *Geological Society of America Abstracts with Programs.* 27(1): 92.

Rezvukhina O.V., Korsakov, A.V., Rezvukhin, D.I., Zamyatin, D.A., Zelenovskiy, P.S., Greshnyakov, E.D., & Shur, V.Y. (2019). A combined Raman spectroscopy, cathodoluminescence, and electron backscatter diffraction study of kyanite porphyroblasts from diamondiferous and diamond-free metamorphic rocks (Kokchetav massif). *J Raman Spectroscopy,* 1–13. https://doi.org/10. 1002/jrs.5757

Rubatto, D. (2002). Zircon trace element geochemistry: partitioning with garnet and the link between U–Pb ages and metamorphism. *Chemical Geology.* 184: 123-138.

Rubatto, D. (2017). Zircon: The Metamorphic Mineral. *Reviews in Mineralogy & Geochemistry*, 83: 261-295.

Rusk, B.G., Lowers, H.A., & Reed, M.H. (2008). Trace elements in hydrothermal quartz: Relationships to cathodoluminescent textures and insights into vein formation. *Geology*, 36(7): 547-550. https://doi.org/10.1130/G24580A.1

Schertl, H.-P., Neuser, R.D., Sobolev, N.V., & Shatsky, V.S. (2004) UHP-metamorphic rocks from Dora Maira/Western Alps and Kokchetav/Kazakhstan: New insights using cathodoluminescence petrography. *European Journal of Mineralogy,* 16: 49-57.

Snoeyenbos, D.R., Koziol, A., Russell, A., Ebel, D.S., and Valley, J.W. (2011) Prograde growth history of possible relic UHP garnets from the Taconian of Western Massachusetts. American Geophysical Union, Fall Meeting 2011, Abstract V21G-04.

Spear, F.S., & Pyle, J.M. (2002) Apatite, Monazite, and Xenotime in Metamorphic Rocks, *Reviews in Mineralogy and Geochemistry* (2002) 48 (1): 293–335. https://doi.org/10.2138/rmg.2002.48.7

Spear, F.S., & Pyle, J.M. (2010) Theoretical modeling of monazite growth in a low-Ca metapelite. *Chemical Geology. 27:* 111-119. doi:10.1016/j.chemgeo.2010.02.016

Spear, F.S. & Wark, D.A. (2009) Cathodoluminescence imaging and titanium thermometry in metamorphic quartz. *Journal of Metamorphic Geology*. 27: 187-205. doi:10.1111/j.1525-1314.2009.00813.x

Spear, F.J. and Wolfe, O. (2020) Revaluation of "equilibrium" P-T paths from zoned garnet in light of quartz inclusion in garnet (QuiG) barometry. *Lithos. 372-373:* 105650.

Spear, F.S. Kohn, M.J., Cheney, J.T., & Florence, F. (2002) Metamorphic, Thermal, and Tectonic Evolution of Central New England. *Journal of Petrology.* 48(11): 2097-2120.

Stanley, R.S. (1964) The bedrock geology of the Collinsville quadrangle, with map. *Connecticut Geological and Natural History Survey, Quadrangle Report 16:* 99 pp.

Stanley, R.S. (1975) Time and Space Relationships of Structures Associated with the Domes of Southwestern Massachusetts and Western Connecticut. In Tectonic Studies of the Berkshire Massif, Western Massachusetts, Connecticut, and Vermont, Geological Survey Professional Paper 888.

Stipp, M., Stünitz, H., Heilbronner, R., & Schmid, S.M. (2002) The eastern Tonale fault zone: a 'natural laboratory' for crystal plastic deformation of quartz over a temperature range from 250 to 700°C. *Journal of Structural Geology.* 24(12):1861-1884. https://doi.org/10.1016/S0191-8141(02)00035-4

Sullivan, W.A., & Peterman, E.M., 2017, Pulverized granite at the brittle-ductile transition: An example from the Kellyland fault zone, eastern Maine, U.S.A. *Journal of Structural Geology.* 101: 109–123. http://dx.doi.org/10.1016/j.jsg.2017.07.002

Tarantola, A., Voudouris, P., Eglinger, A., Scheffer, C., Trebus, K., Bitte, M., Rondeau, B., Mavrogonatos, C., Graham, I., Etienne, M., & Peiffert, C. (2019) Metamorphic and Metasomatic Kyanite-Bearing Mineral Assemblages of Thassos Island (Rhodope, Greece). *Minerals.* 9(4): 252. https://doi.org/10.3390/min9040252

Taylor, R.J.M., Kirkland, C.L., & Clark, C. (2016) Accessories after the facts: Constraining the timing, duration, and conditions of high-temperature metamorphic processes. *Lithos.* 264: 239-257. http://dx.doi.org/10.1016/j.lithos.2016.09.004

Thomas, J.B., Watson, E.B., Spear, F.S., Shemella, P.T., Nayak, S. K., & Lanzirotti, A. (2010) TitaniQ under pressure: the effect of pressure and temperature on the solubility of Ti in quartz. *Contributions to Mineralogy and Petrology.* DOI 10.1007/s00410-010-0505-3

Thomas, J.B., Watson, E.B., Spear, F.S., & Wark, D.A. (2015) TitaniQ recrystallized: experimental confirmation of the original Ti-in-quartz calibrations. *Contributions to Mineralogy and Petrology.* 169: 27, doi:10.1007/s00410-015-1120-0

Thompson, A.B., Tracy, R.J., Lyttle, P.T. and Thompson, J.B., Jr. (1977) Prograde reaction histories deduced from compositional zonation and mineral inclusions in garnet from Gassetts schist, Vermont. *American Journal of Science*, 277: 1152-1167.

Vance, D. & Holland, T. (1993) A detailed isotopic and petrological study of a single garnet from the Gassetts Schist, Vermont. *Contributions to Mineralogy and Petrology.* 114: 101-118.

Wark, D.A. & Spear, F.S. (2005) Titanium in quartz: cathodoluminescence and thermometry. *Geochimica et Cosmochimica Acta.* Suppl 69: A592

Wark, D.A. & Watson, E.B. (2006) TitaniQ: a titanium-in-quartz geothermometer. *Contributions to Mineralogy and Petrology.* 152: 743-754. DOI 10.1007/s00410-006-0132-1

Whitney, D.L. & Evans, B.W. (2010) Abbreviations for names of rock-forming minerals. *American Mineralogist.* 95: 185–187. DOI: 10.2138/am.2010.3371

Wiebe, R.A., Wark, D.A., & Hawkins, D.P. (2007). Insights from quartz cathodoluminescence zoning into crystallization of the Vinalhaven granite, coastal Maine. *Contributions to Mineralogy and Petrology.* 154: 439-453. DOI 10.1007/s00410-007-0202-z

Wojtowicz, A.J. (1991) Luminescence of Cr3+ in kyanite. *Journal of Luminescence.* 50(4): 221-230. https://doi.org/10.1016/0022-2313(91)90046-X

Wojtowicz, A.J., Grinberg, M. & Lempicki, A. (1991) The coupling of $^4T_2$ and ^2E states of the Cr^{3+} ion in solid state materials. *Journal of Luminescence.* 50(4): 231-242. https://doi.org/10.1016/0022-2313(91)90047-Y

Yang, P. & Rivers, T. (2001) Chromium and manganese zoning in pelitic garnet and kyanite: Spiral, overprint, and oscillatory (?) zoning patterns and the role of growth rate. *Journal of Metamorphic Geology.* 19: 455-474.

Zhang, R. Y., Liou, J. G., Omori, S., Sobolev, N. V., Shatsky, V. S., Iizuka, Y., Lo, C. H., & Ogasawara, Y. (2012). Tale of the Kulet eclogite from the Kokchetav Massive, Kazakhstan: Initial tectonic setting and transition from amphibolite to eclogite. *Journal of Metamorphic Geology*, *30*(5), 537-559. https://doi.org/10.1111/j.1525-1314.2012.00980.x

FIGURE CAPTIONS

Figure 1. Cathodoluminescence (CL) images of kyanite from the Goshen Dome (a-d) and Rhodope localities (e-h). In Color CL mode, the signal is split into red, green, and blue channels using dichroic filters; the Color CL image is a composite of these channels.

Figure 2. CL images of kyanite. a) Kyanite hosted by garnet from the Rhodope Metamorphic Complex at the Xanthi locality. b) Kyanite porphyroblast from the Kokchetav UH*P* whiteschist. c) Kyanite from the Xanthi locality, featuring four CL textures. d-e) Kyanite from the (U)H*P* Goshen Dome locality within the Northern Appalachians. f-g) Kyanite from the Gassetts Schist locality within the Northern Appalachians. Note the overall lower intensity of CL color, apart from the CL-bright rim that partially surrounds the grain. h) Kyanite from the RMC, Xanthi locality. i) Kyanite porphyroblasts from the Straits Schist, located in the Northern Appalachians. Mineral abbreviations after Whitney and Evans (2010).

Figure 3. CL images and EPMA maps of Fe, P and Mg. a-d) Representative grain from the Goshen Dome locality within the Northern Appalachians. Yellow arrows mark sector boundaries evident in the CL image and some of the compositional maps. See text for discussion. White arrows mark CL-bright features that are not evident in the compositional maps. e-h) Representative kyanite from the Xanthi locality of the Rhodope Metamorphic Complex. Yellow arrows mark steep increases in P concentration; corresponding arrows in CL image and Mg and Fe maps do not exhibit uniformly similar trends.

Figure 4. Representative kyanite porphyroblast from the Goshen Dome locality. a) Color CL image. Numbers correspond to EPMA analysis locations. Letters correspond to transects; open circles mark the start and closed circles mark the end of each transect. b-d) EPMA maps of Fe, P and Mg; white dotted line marks central domain. e) Schematic diagram identifying different domains. f) Quantitative point analyses

(in ppm) with 1σ uncertainties. Fe plotted on the right y-axis; Mg and P plotted on the left y-axis. Shading corresponds to schematic sketch. g-h) Transects across CL domains. Ti and Zr plotted on the left y-axis; Cr_2O_3 plotted on the right y-axis. Lower panels show signal intensities measured on the red, green, and blue channels of the Color CL detector along each transect.

Figure 5. Representative kyanite porphyroblast from the Goshen Dome locality. a-b) Photomicrographs in plane (PPL) and cross-polarized light (XPL), respectively. Kink bands and undulatory extinction are evident in XPL. c) CL image of the porphyroblast. Numbers correspond to transects; open circles mark the start and closed circles mark the end of each transect. d-e) EPMA maps of Fe and P of region outlined in yellow in c. f-g) Ti and Zr plotted on the left y-axis; Cr plotted on the right y-axis. Lower panels show signal intensities measured on the red, green, and blue channels of the Color CL detector along each transect.

Figure 6. CL images of representative kyanite from the Rhodope Metamorphic Complex. a-c) Matrix porphyroblasts. d) Kyanite hosted by garnet porphyroblasts. E) Quantitative point analyses with 1σ uncertainties. FeO plotted on the right y-axis; all other oxides plotted on the left y-axis. Shaded regions correspond to analyses from CL-dark domains; non-shaded regions correspond to CL-bright domains.

Figure 7. Representative kyanite porphyroblast from Kokchetav. a) CL image. b) EBSD map with Inverse Pole Figure (IPF) z coloring. c) Misorientation with respect to the crystallographic orientation at the red cross. Yellow-to-green region (upper left) transitions sharply into blue along a kyanite twin. d) Pole figures (lower hemisphere, equal area) of {100}, <010> and {001} show rotation about <010> and dispersion along {100} and {001}, consistent with a (100)[001] slip system. Upper hemisphere projection of <010> not shown; exclusively contains data from the kyanite twin. Black dot marks the pole to the great circle

(dashed line) that fits a large subset of the data. Colors are consistent with IPF z in b. Data from the kyanite twin plot beneath the blue and purple data in {100} and are marked in {001}. e) Schematic diagram shows relevant planes, directions and axes.

Figure 8. Representative kyanite porphyroblasts from Rhodope. a) EBSD map with IPF x coloring overlaid on band contrast (BC). b) CL image shows locations of kink bands and the bent crystal form. c) Pole figures of {100}, <010> and {001} show rotation about <010> and dispersion along {100} and {001}, consistent with a (100)[001] slip system. d) Schematic diagram shows relevant planes, directions, and axes.

Figure 9. Representative kyanite porphyroblasts from the Northern Appalachians. a) EBSD map of IPF z overlaid on band contrast. b) CL image. c) Pole figures of <010> on the left; {100} and {001} on the right. Data indicate rotation about <010> and dispersion along {100} and {001}, consistent with a (100)[001] slip system. Data from the "red grain" are red; data from the "blue grain" are green and blue. Great circles that fit {100} {001} for each grain shown as dotted lines; poles to these great circles are marked as dots. d) Schematic diagrams of each kyanite show relevant planes, directions and axes. e-f) EBSD maps from the kyanite porphyroblasts in Fig. 4; coloring in E is IPF z; coloring in F is misorientation with respect to the crystallographic orientation at the red cross; yellow box corresponds to area mapped by EPMA (Fig. 4d,e). g) Pole figure coloring corresponds to IPF z; data indicate rotation about <010> with dispersion along {100} and {001}, consistent with a (100)[001] slip system. A great circle drawn through most of the data (thin grey line) and its corresponding pole (black dot). h) Schematic diagram shows relevant planes, directions and axes. i) CL image of kyanite from the Gassetts Schist. j) EBSD map of misorientation of the crystallographic orientation with respect to the red cross. k) Pole figures show clustering of <010> and minimal dispersion of {100} and {001}. L) Schematic diagram shows relevant planes, directions and axes.

Table Caption

Table 1: Detection limits for EPMA analytical sessions

Figure 1

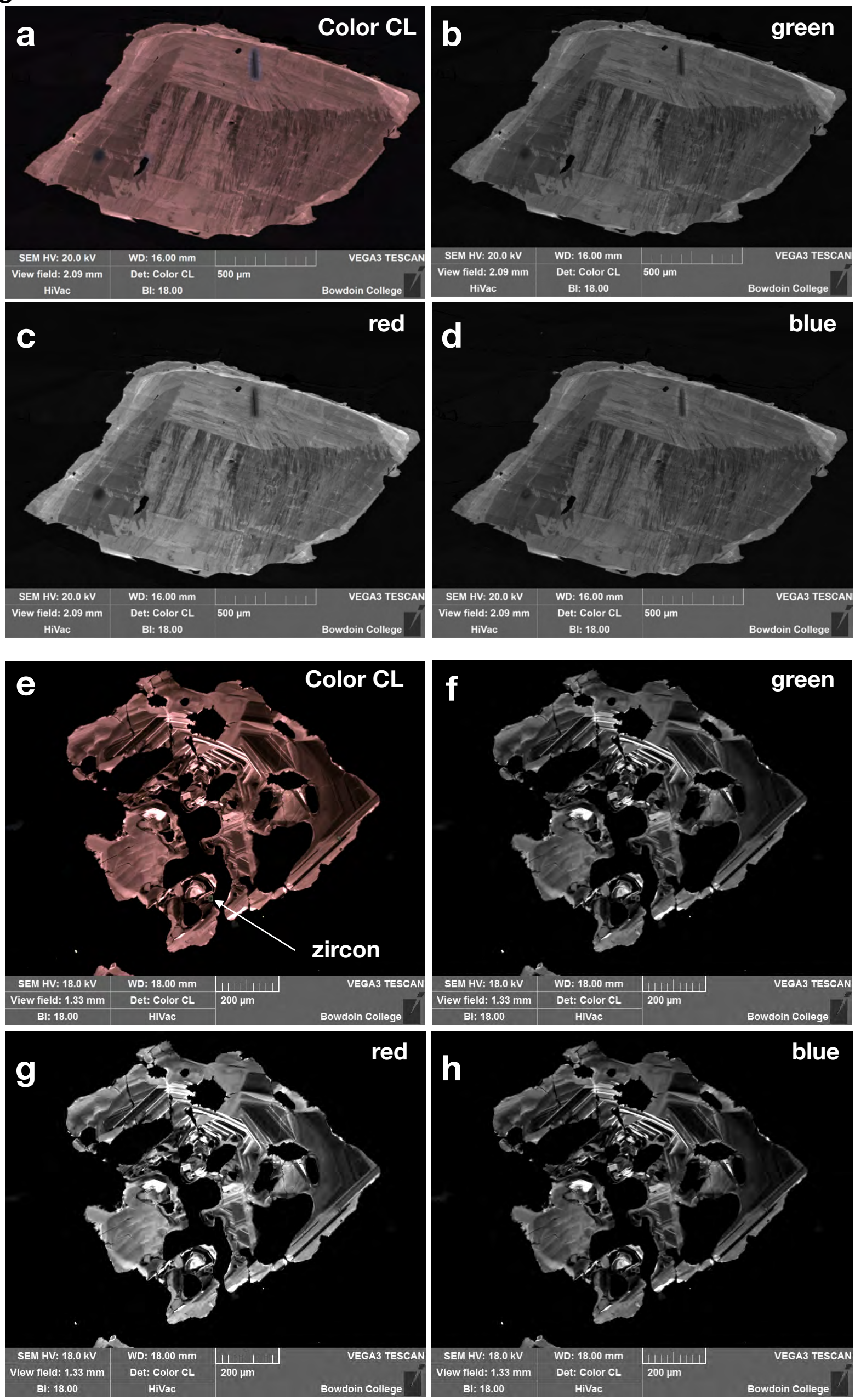
a
Color CL
SEM HV: 20.0 kV
WD: 16.00 mm
VEGA3 TESCAN
View field: 2.09 mm
Det: Color CL
500 µm
HiVac
BI: 18.00
Bowdoin College
b
green
SEM HV: 20.0 kV
WD: 16.00 mm
VEGA3 TESCAN
View field: 2.09 mm
Det: Color CL
500 µm
HiVac
BI: 18.00
Bowdoin College
c
red
SEM HV: 20.0 kV
WD: 16.00 mm
VEGA3 TESCAN
View field: 2.09 mm
Det: Color CL
500 µm
HiVac
BI: 18.00
Bowdoin College
d
blue
SEM HV: 20.0 kV
WD: 16.00 mm
VEGA3 TESCAN
View field: 2.09 mm
Det: Color CL
500 µm
HiVac
BI: 18.00
Bowdoin College
e
Color CL
zircon
SEM HV: 18.0 kV
WD: 18.00 mm
VEGA3 TESCAN
View field: 1.33 mm
Det: Color CL
200 µm
BI: 18.00
HiVac
Bowdoin College
f
green
SEM HV: 18.0 kV
WD: 18.00 mm
VEGA3 TESCAN
View field: 1.33 mm
Det: Color CL
200 µm
BI: 18.00
HiVac
Bowdoin College
g
red
SEM HV: 18.0 kV
WD: 18.00 mm
VEGA3 TESCAN
View field: 1.33 mm
Det: Color CL
200 µm
BI: 18.00
HiVac
Bowdoin College
h
blue
SEM HV: 18.0 kV
WD: 18.00 mm
VEGA3 TESCAN
View field: 1.33 mm
Det: Color CL
200 µm
BI: 18.00
HiVac
Bowdoin College

Figure 2

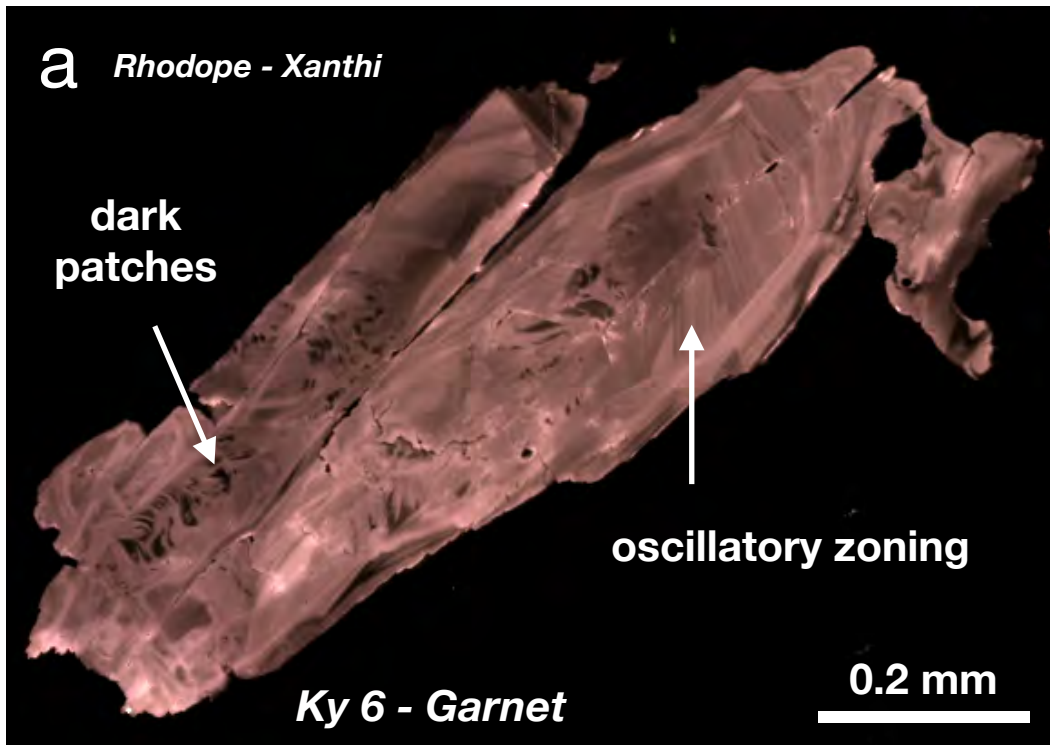
a
Rhodope - Xanthi
dark patches
oscillatory zoning
Ky 6 - Garnet
0.2 mm

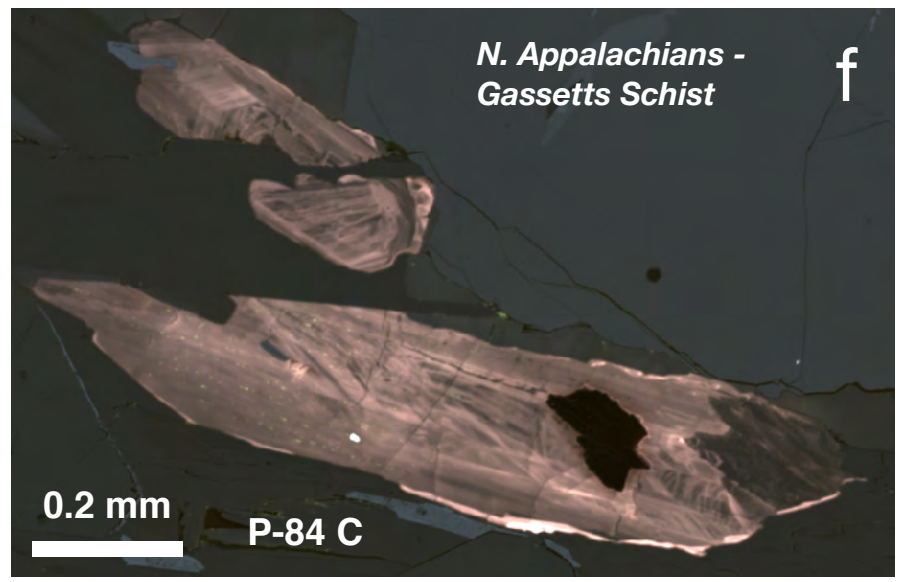
N. Appalachians - Gassetts Schist
f
0.2 mm
P-84 C

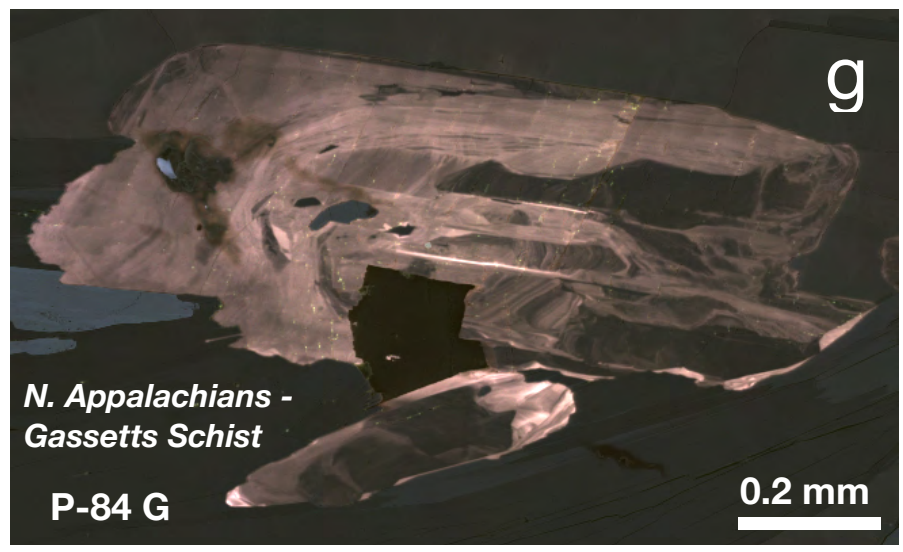
g
N. Appalachians - Gassetts Schist
P-84 G
0.2 mm

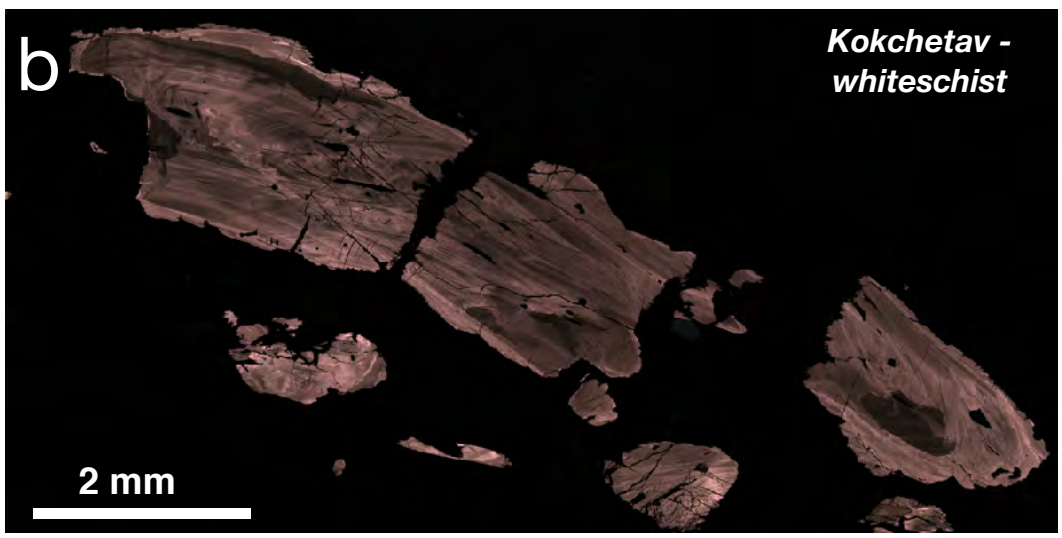
b
Kokchetav - whiteschist
2 mm

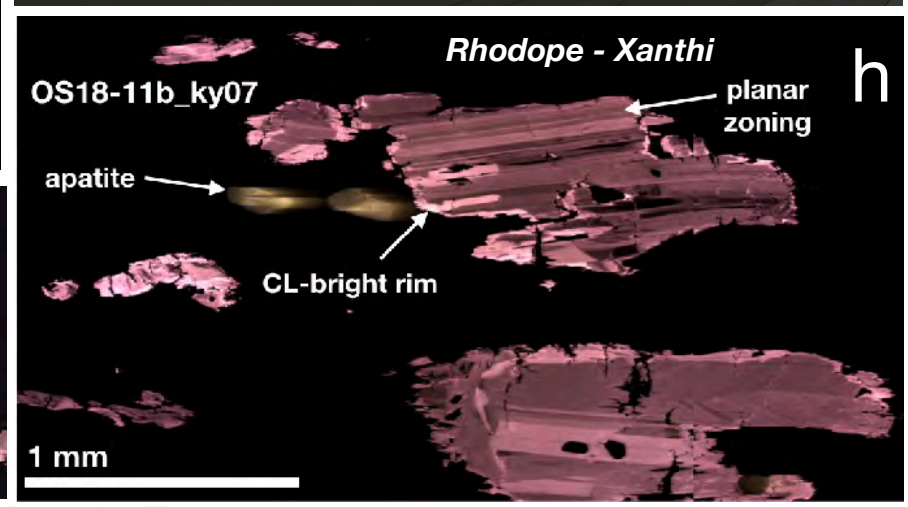
Rhodope - Xanthi
h
OS18-11b_ky07
planar zoning
apatite
CL-bright rim
1 mm

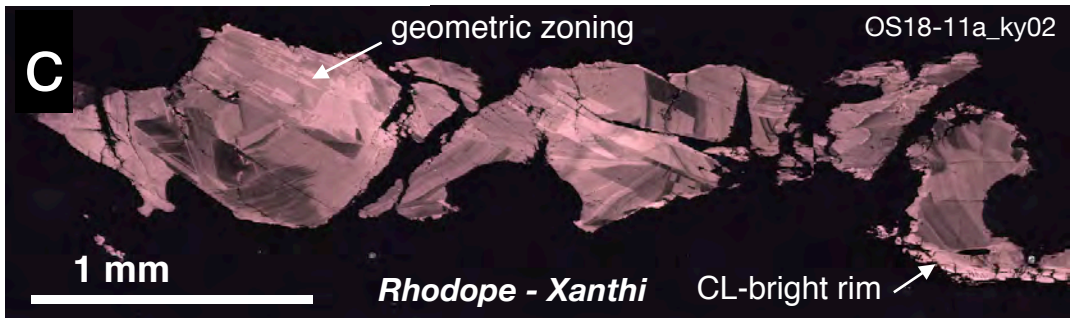
c
geometric zoning
OS18-11a_ky02
1 mm
Rhodope - Xanthi
CL-bright rim

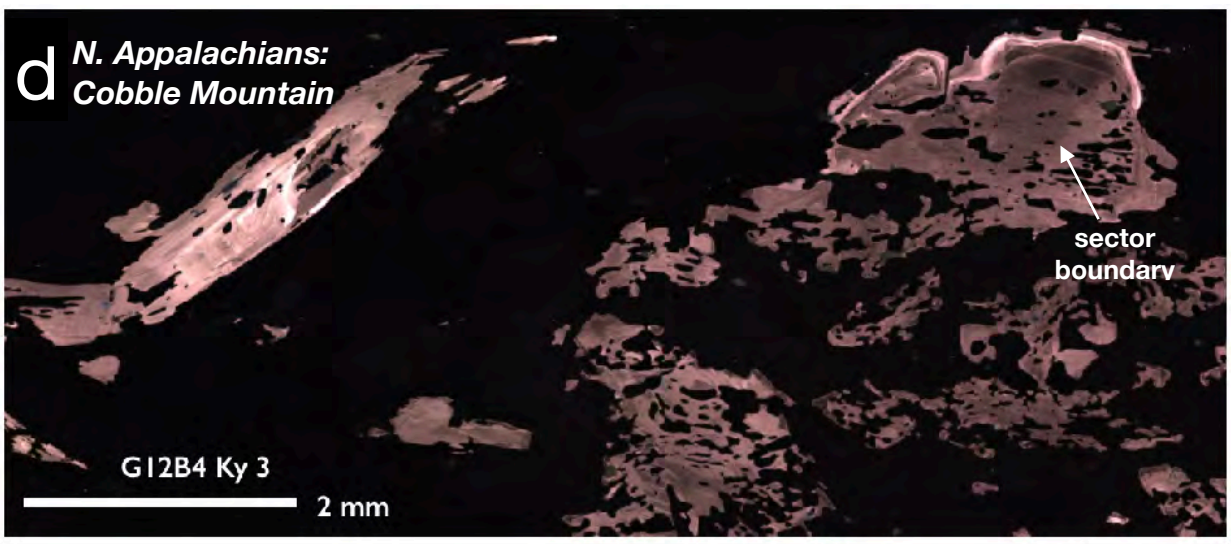
d
N. Appalachians: Cobble Mountain
sector boundary
G12B4 Ky 3
2 mm

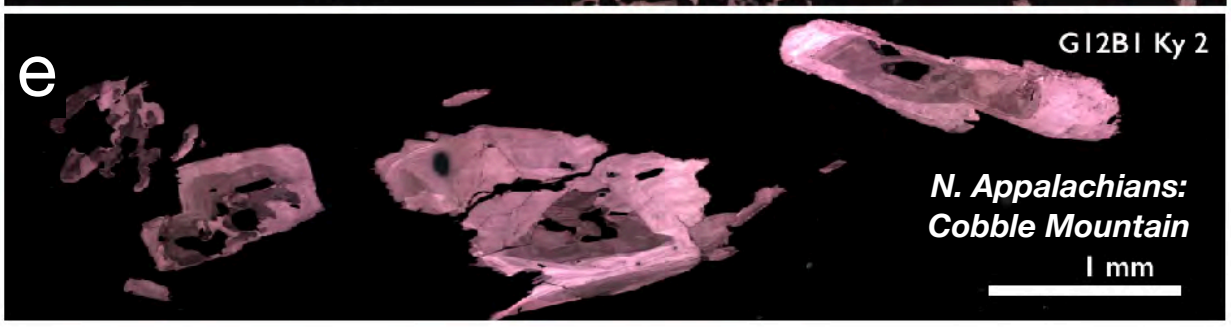
e
G12B1 Ky 2
N. Appalachians: Cobble Mountain
1 mm


N. App. Straits Schist
i
1 mm
P-1156 Ky 2

Figure 3

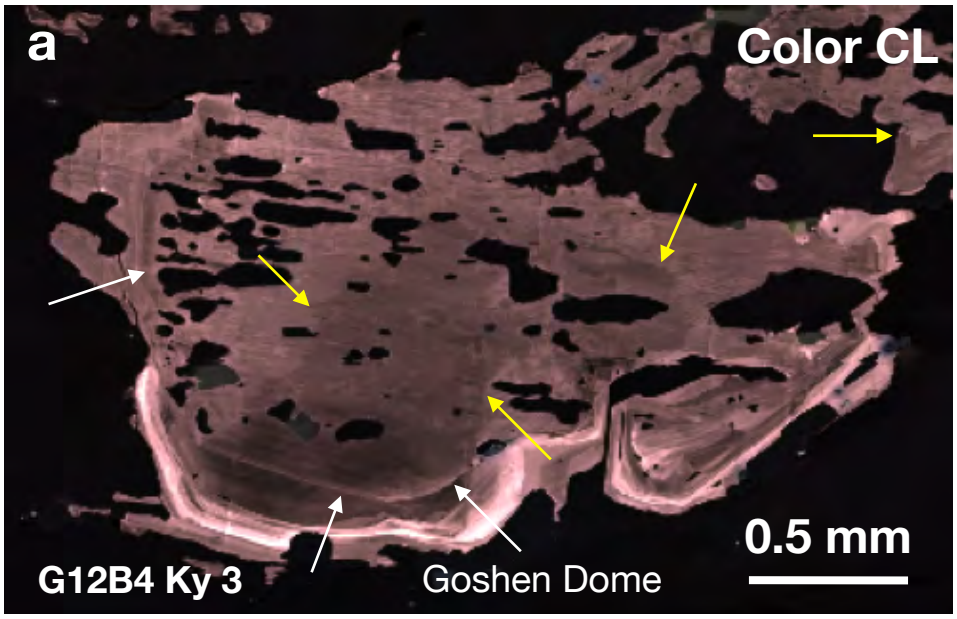
a
Color CL
G12B4 Ky 3
Goshen Dome
0.5 mm

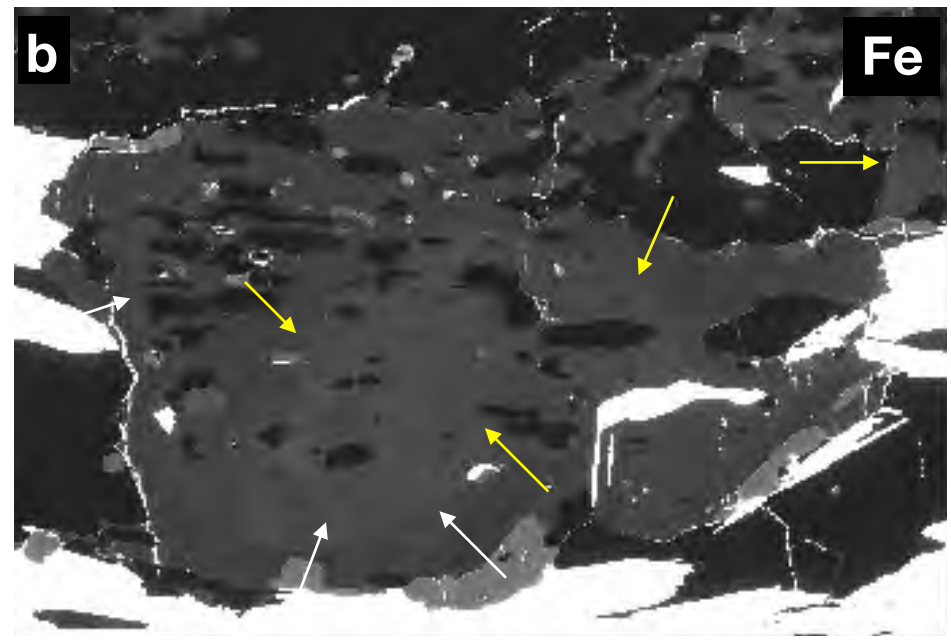
b
Fe

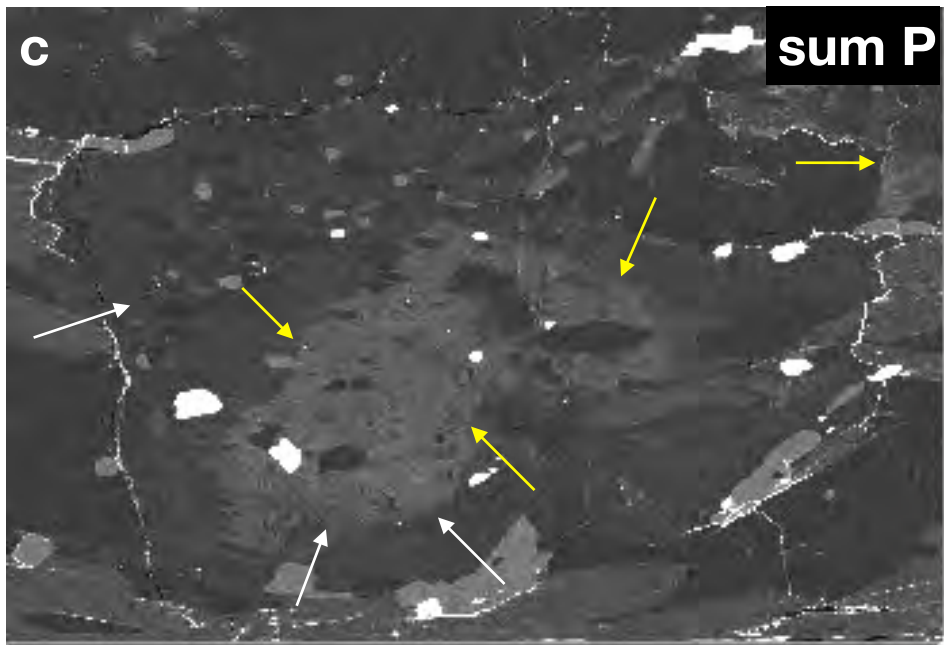
c
sum P

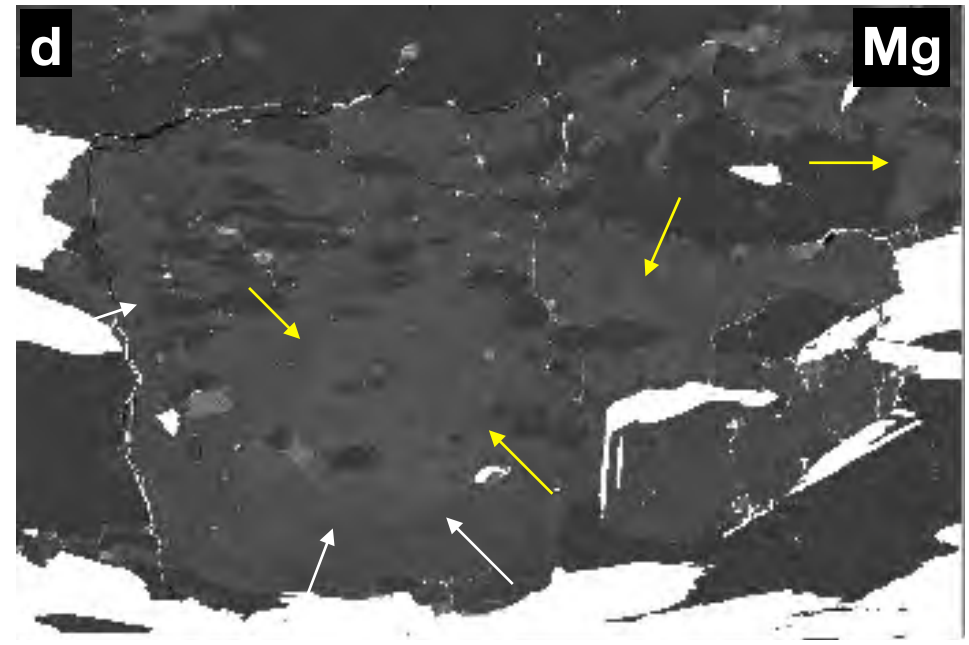
d
Mg

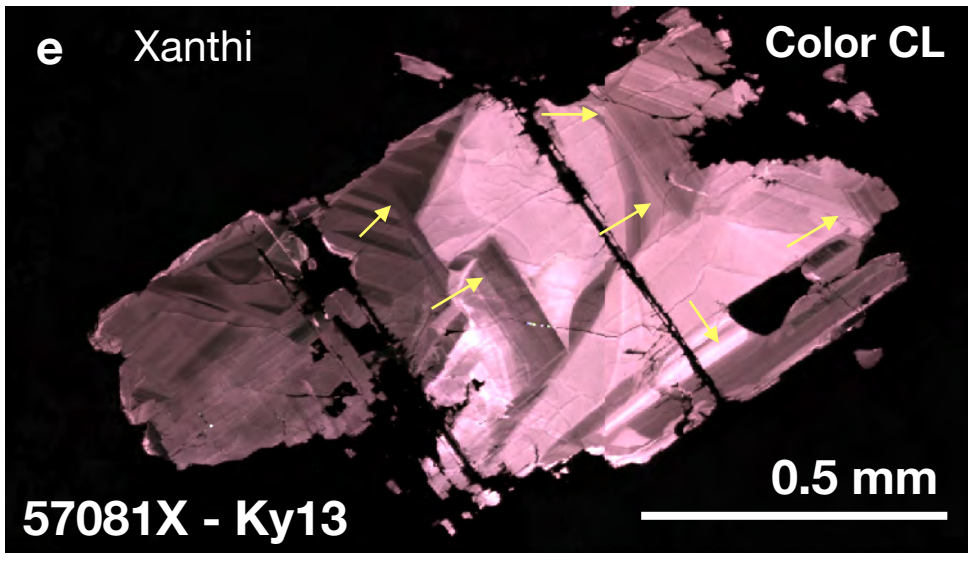
e
Xanthi
Color CL
57081X - Ky13
0.5 mm

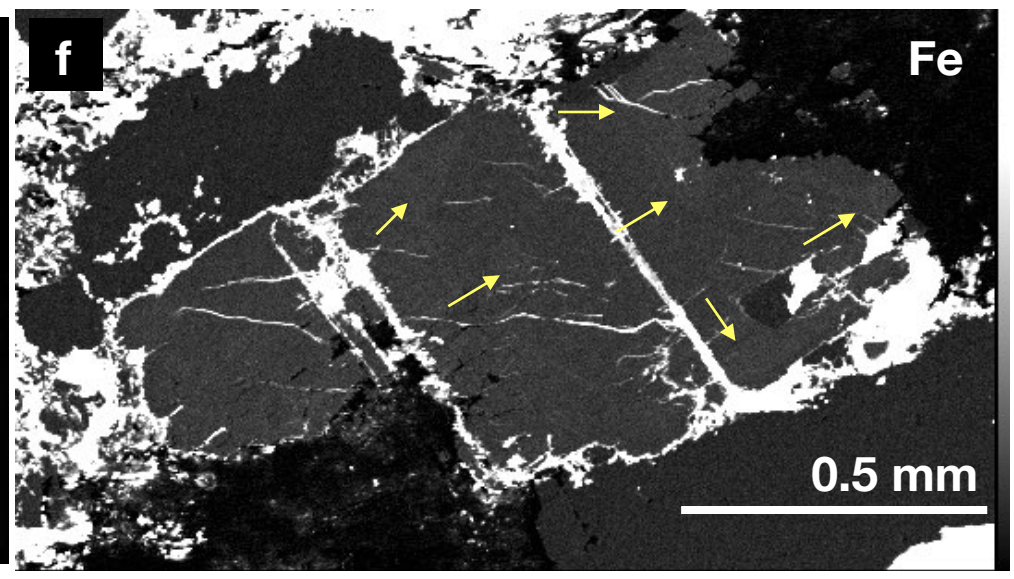
f
Fe
0.5 mm

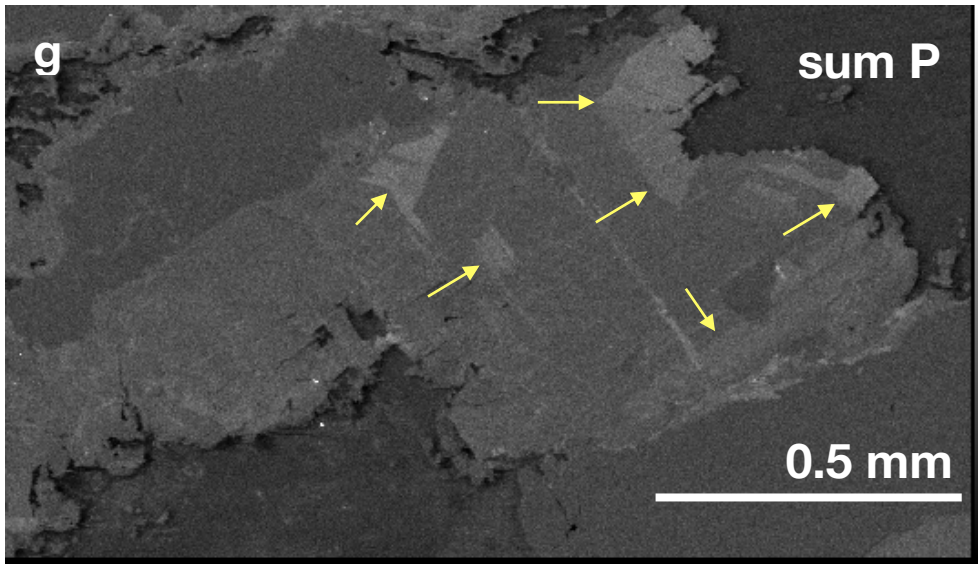
g
sum P
0.5 mm

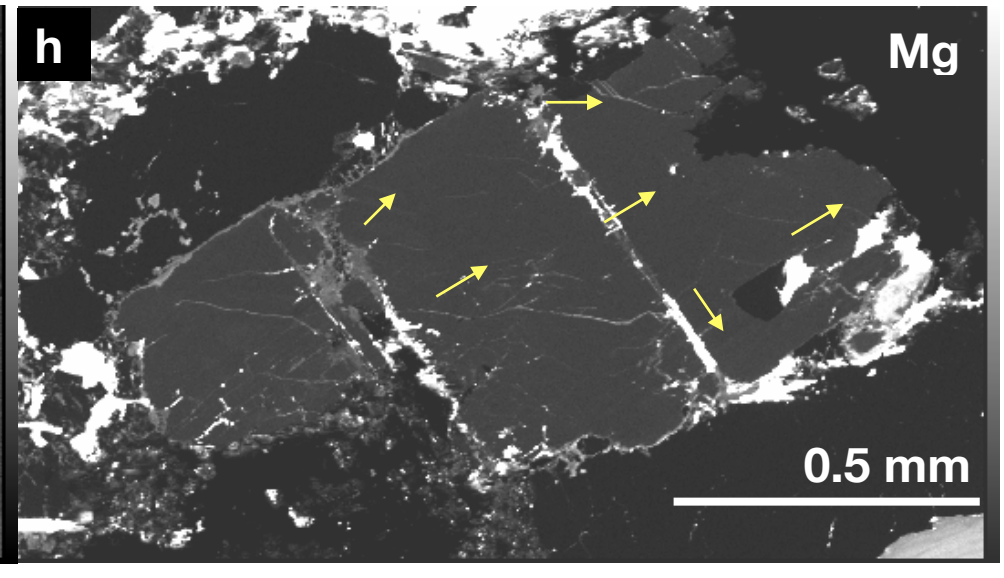
h
Mg
0.5 mm

Figure 4

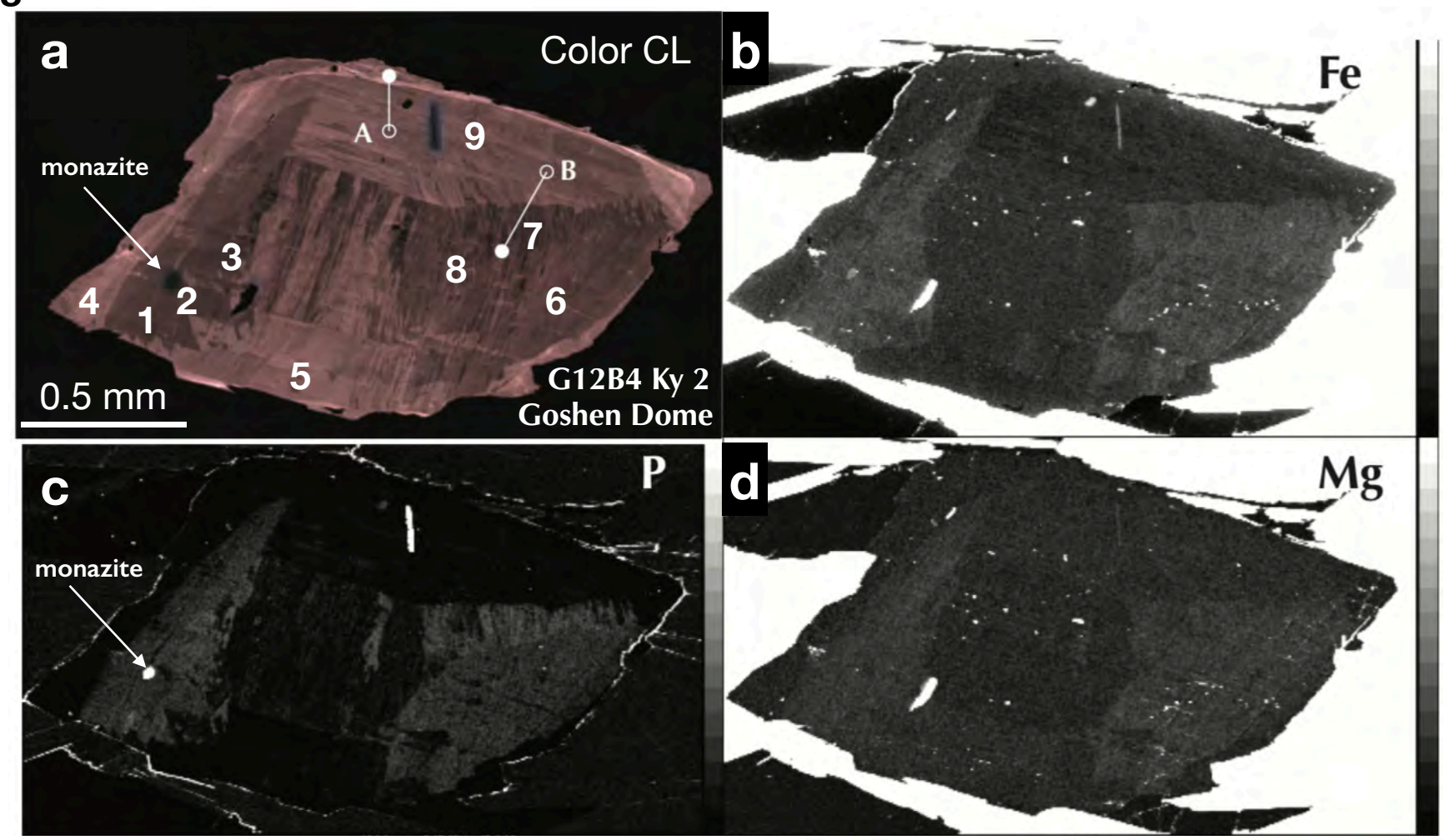
a
Color CL
monazite
A
B
1
2
3
4
5
6
7
8
9
0.5 mm
G12B4 Ky 2
Goshen Dome
b
Fe
c
P
monazite
d
Mg

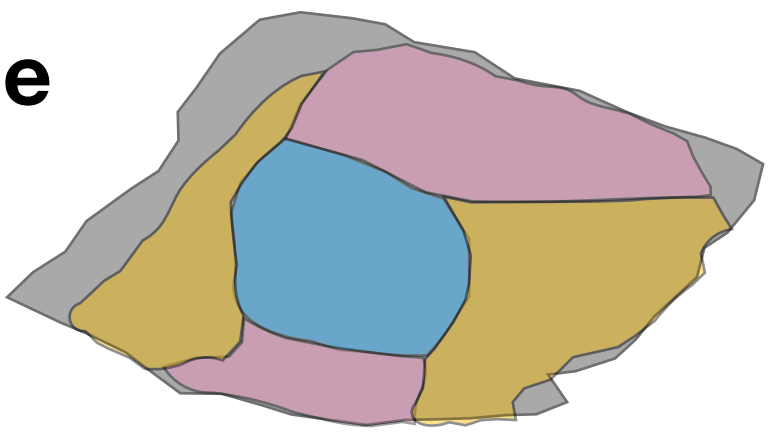
e

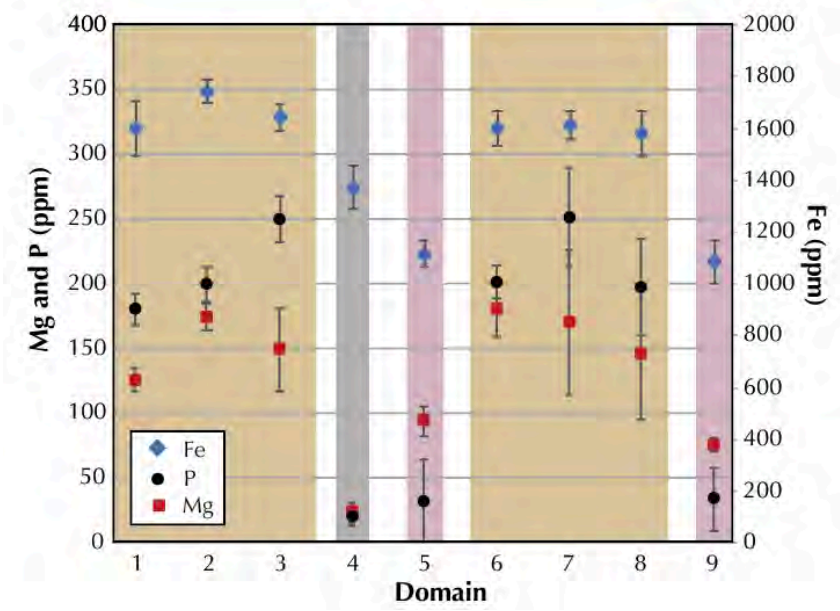
f
Mg and P (ppm)
Fe (ppm)
Fe
P
Mg
Domain

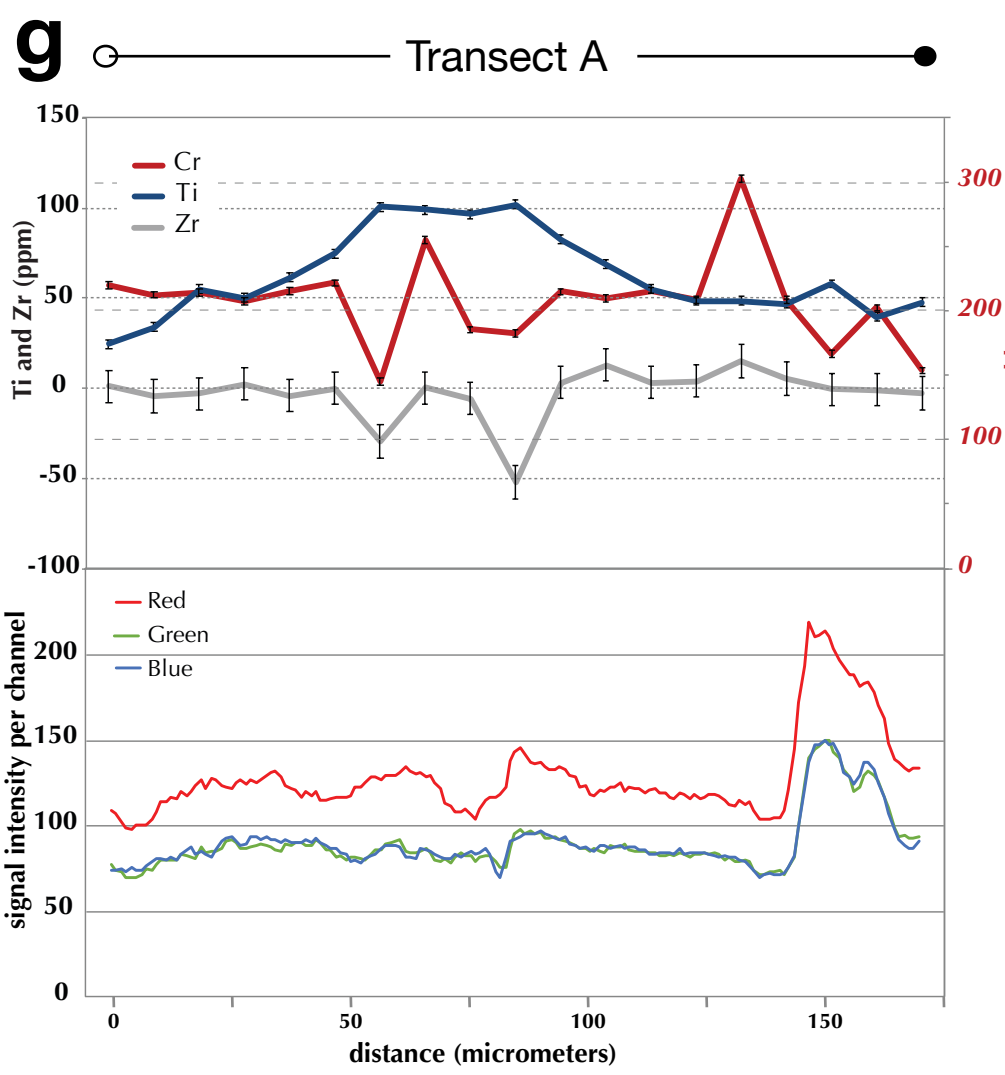
g
Transect A
Cr
Ti
Zr
Ti and Zr (ppm)
Cr (ppm)
Red
Green
Blue
signal intensity per channel
distance (micrometers)

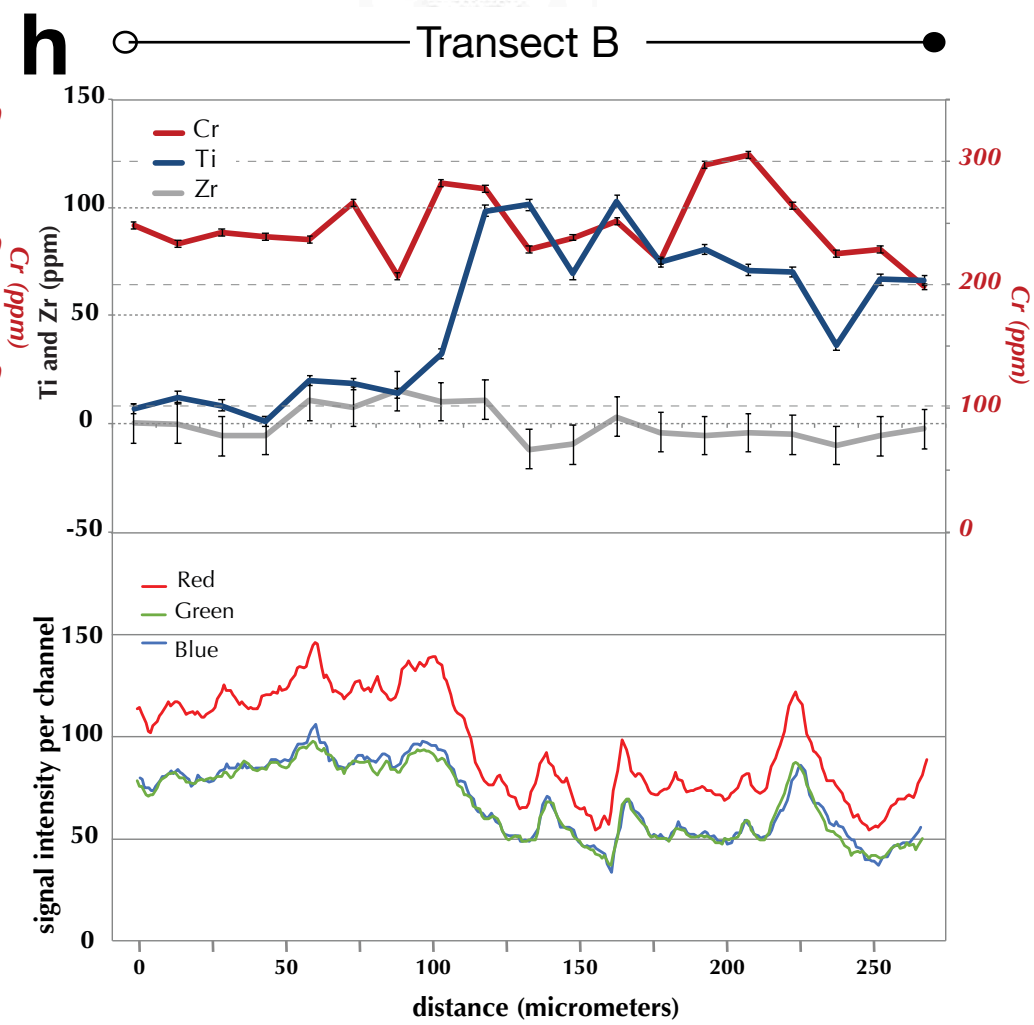
h
Transect B
Cr
Ti
Zr
Ti and Zr (ppm)
Cr (ppm)
Red
Green
Blue
signal intensity per channel
distance (micrometers)

Figure 5

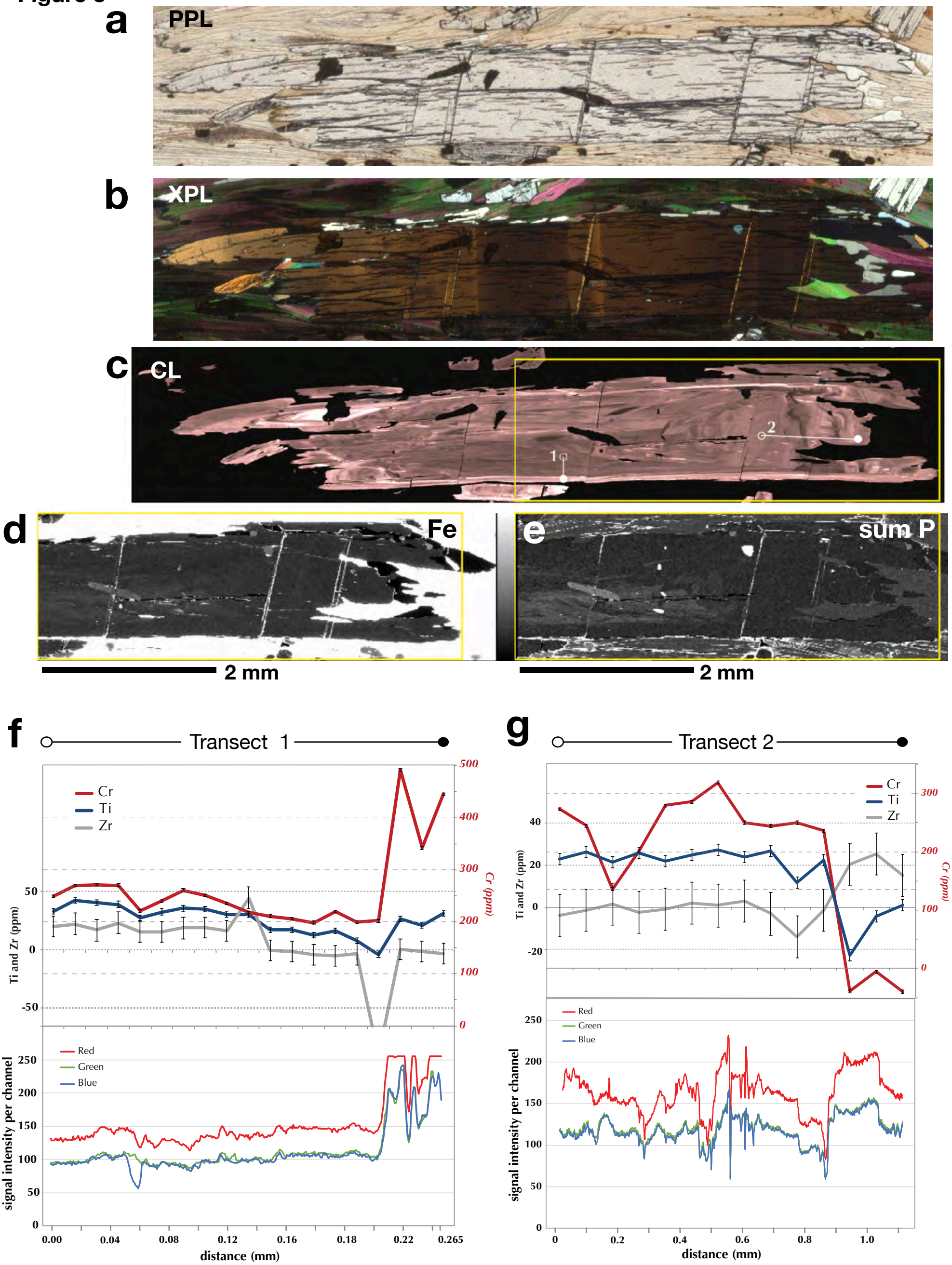
a
PPL
b
XPL
c
CL
1
2
d
Fe
2 mm
e
sum P
2 mm
f
Transect 1
Cr
Ti
Zr
Ti and Zr (ppm)
Cr (ppm)
Red
Green
Blue
signal intensity per channel
distance (mm)
g
Transect 2
Cr
Ti
Zr
Ti and Zr (ppm)
Cr (ppm)
Red
Green
Blue
signal intensity per channel
distance (mm)

Figure 6

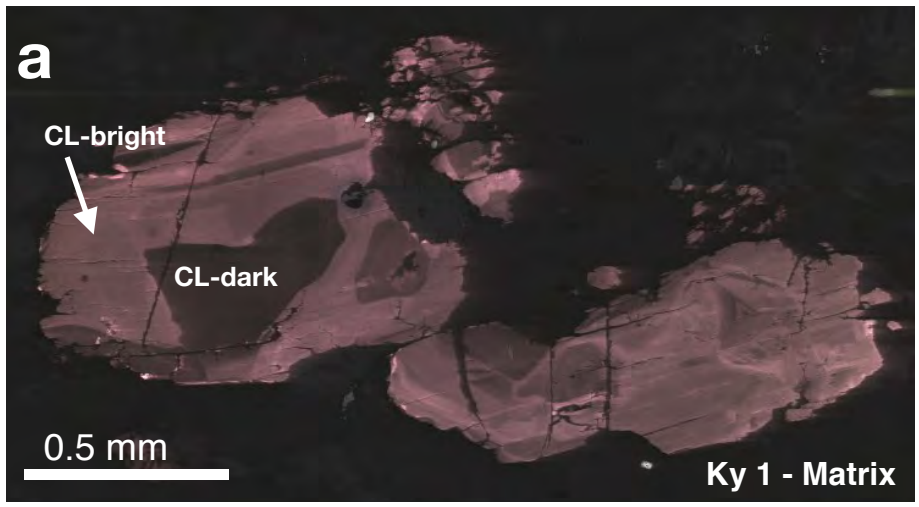
a
CL-bright
CL-dark
0.5 mm
Ky 1 - Matrix

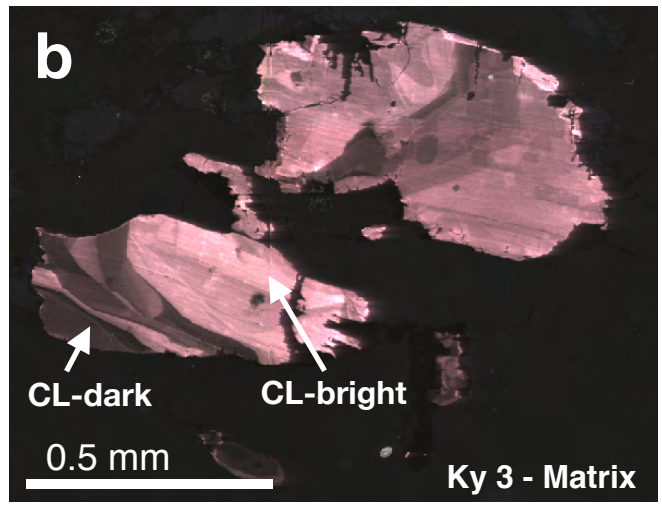
b
CL-dark
CL-bright
0.5 mm
Ky 3 - Matrix

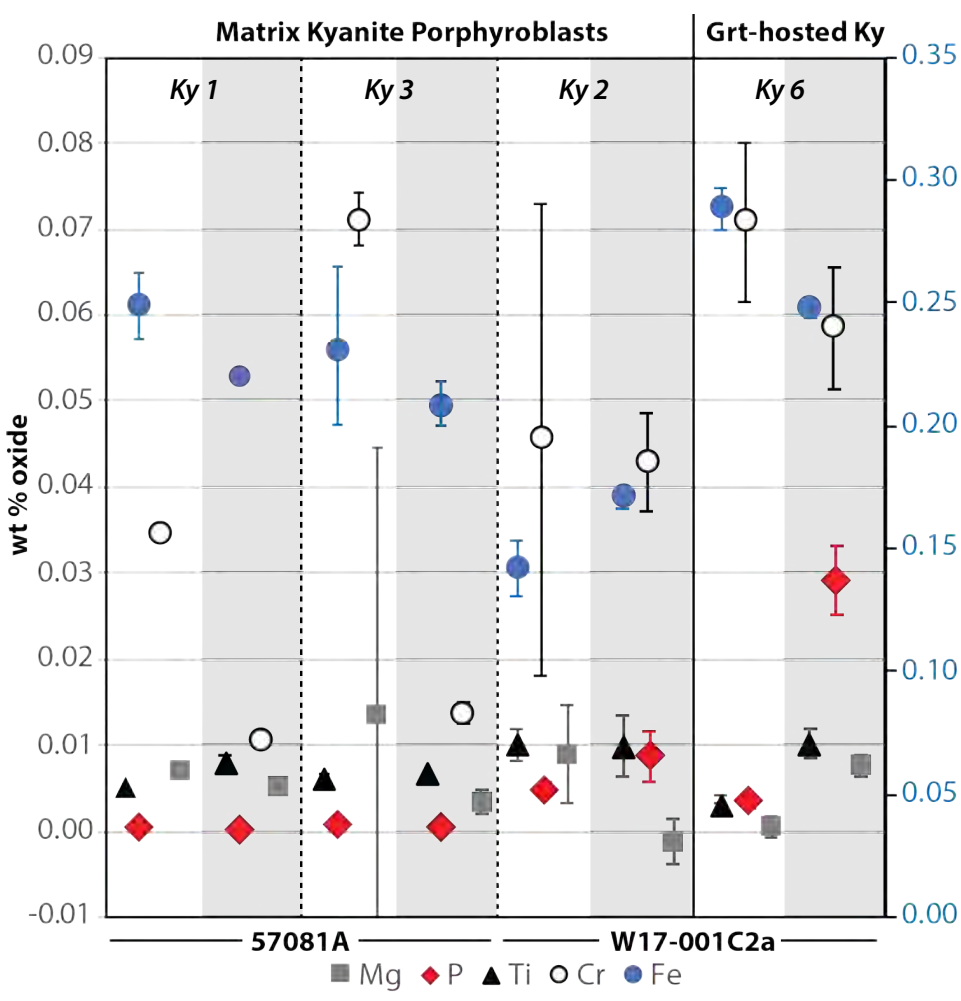
e - EPMA results
Matrix Kyanite Porphyroblasts
Grt-hosted Ky
Ky 1
Ky 3
Ky 2
Ky 6
wt % oxide
wt % FeO
0.09
0.08
0.07
0.06
0.05
0.04
0.03
0.02
0.01
0.00
-0.01
0.35
0.30
0.25
0.20
0.15
0.10
0.05
0.00
57081A
W17-001C2a
Mg P Ti Cr Fe

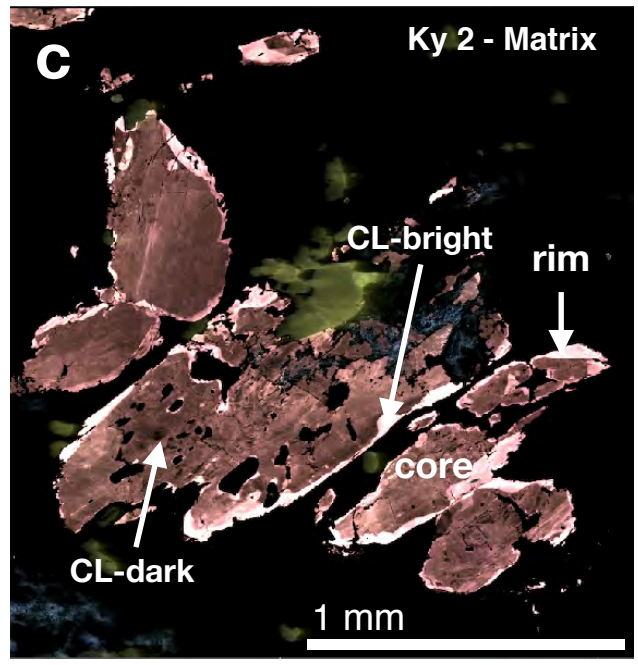
c
Ky 2 - Matrix
CL-bright
rim
core
CL-dark
1 mm

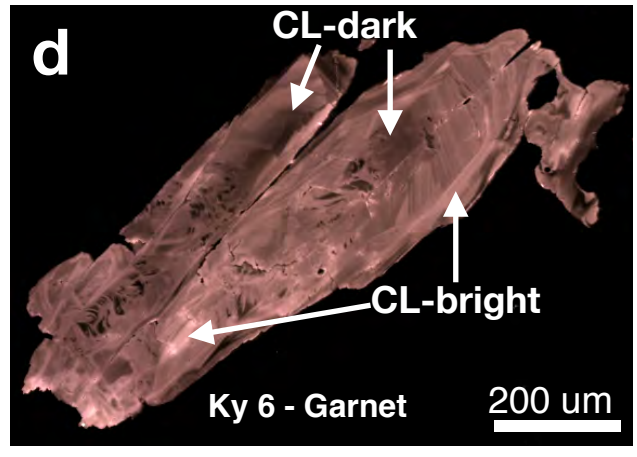
d
CL-dark
CL-bright
Ky 6 - Garnet
200 um

Figure 7

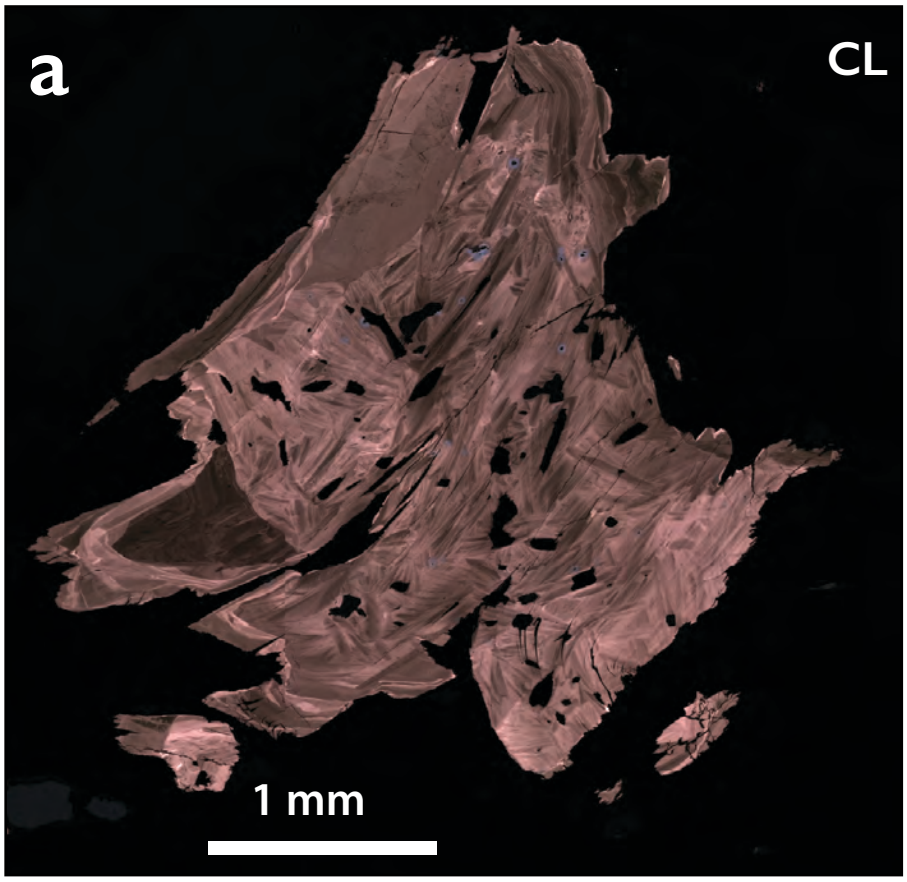
a
CL
1 mm

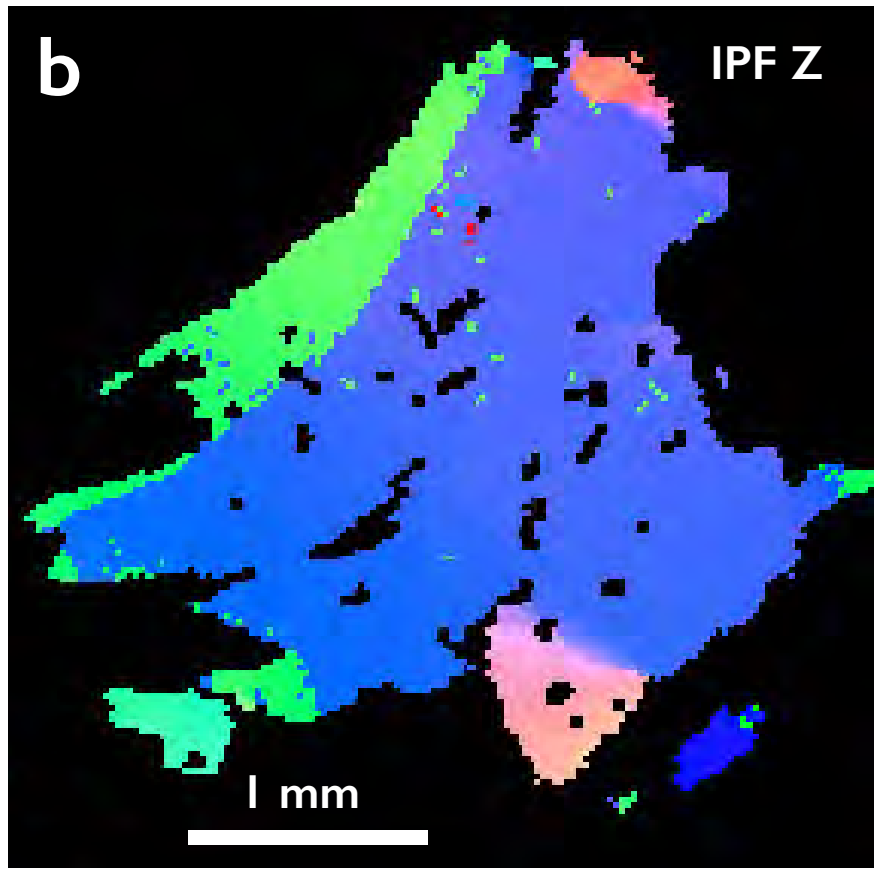
b
IPF Z
1 mm

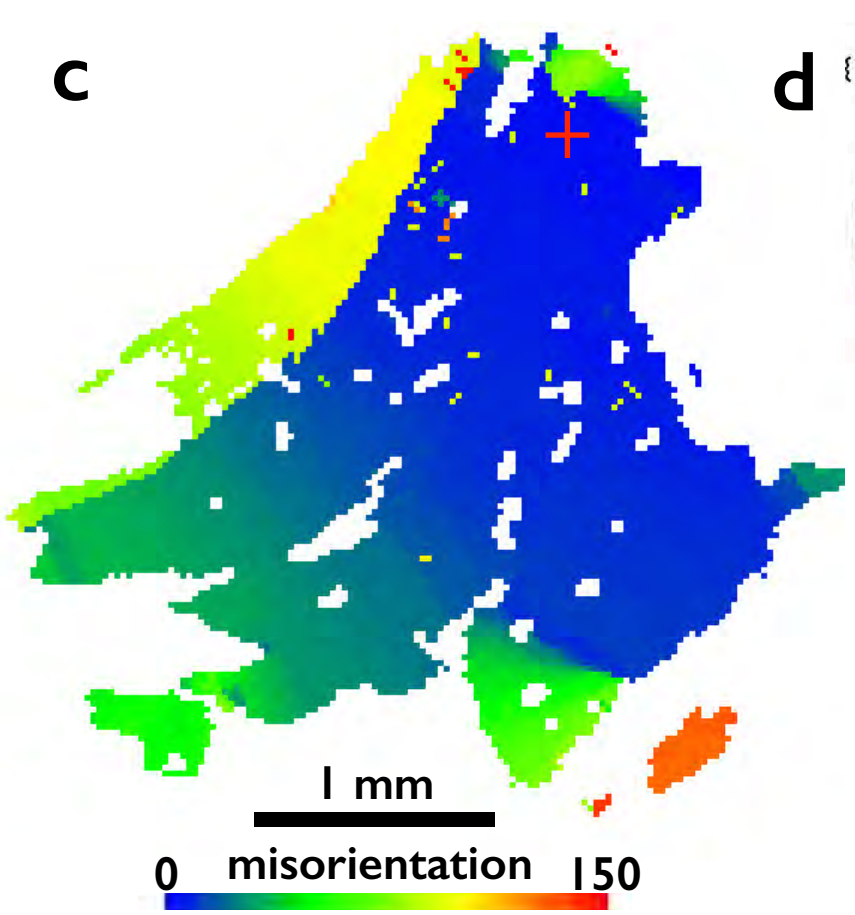
c
1 mm
0
misorientation
150

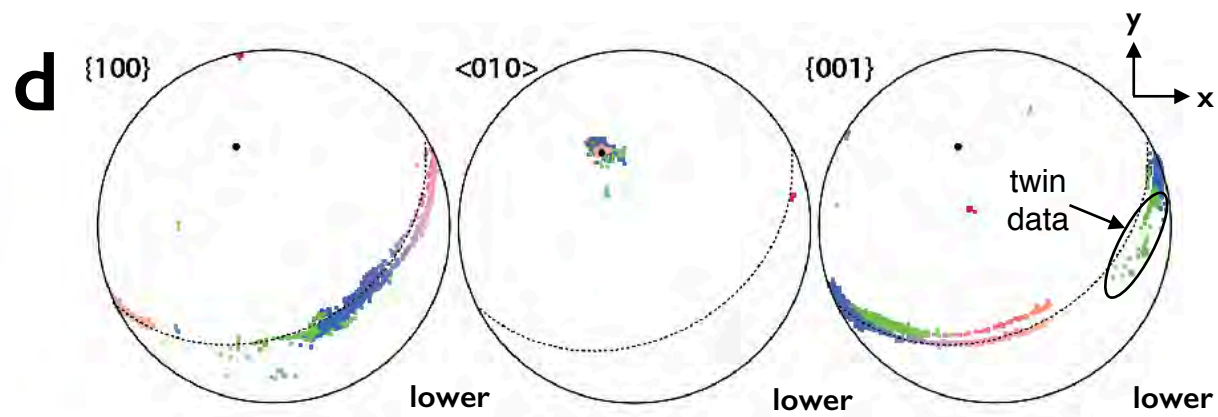
d
{100}
<010>
{001}
y
x
twin
data
lower
lower
lower

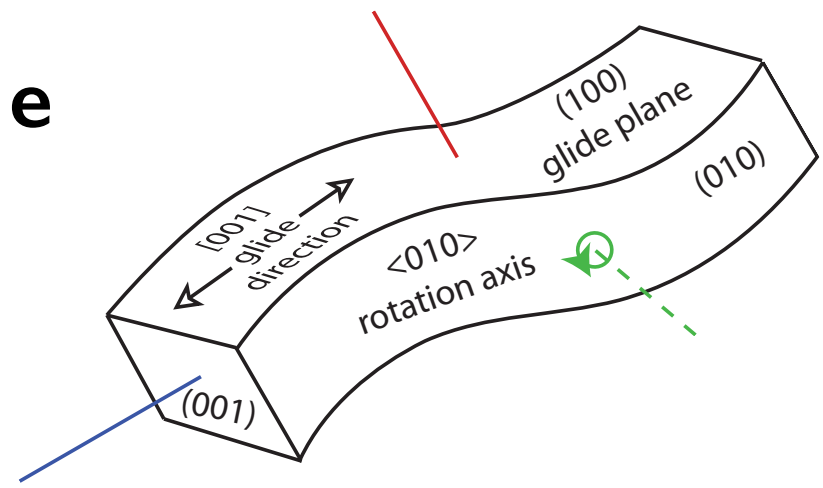
e
(100)
glide plane
(010)
[001]
glide
direction
<010>
rotation axis
(001)

Figure 8

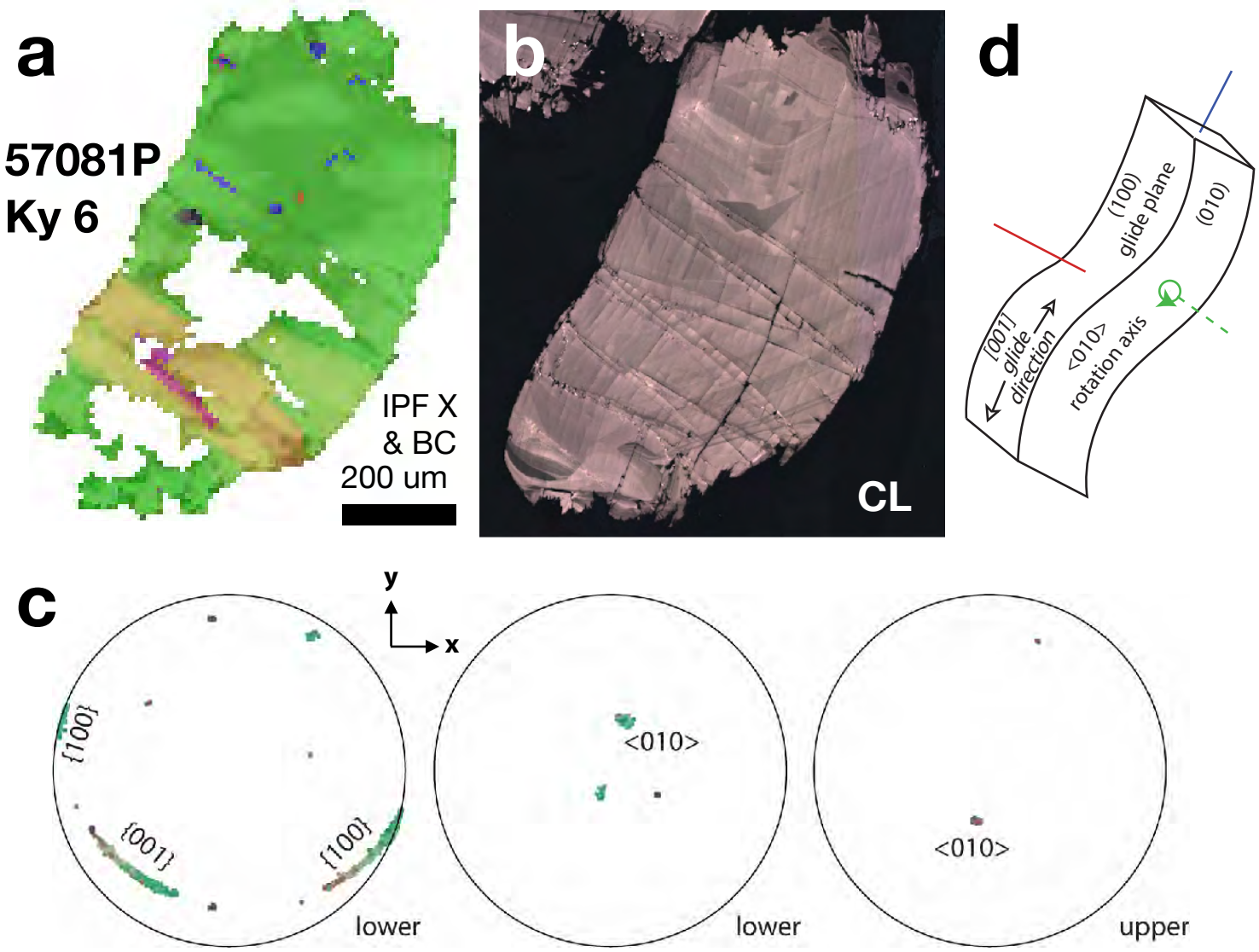
a
57081P
Ky 6
IPF X
& BC
200 um
b
CL
d
(100)
glide plane
(010)
[001]
glide
direction
<010>
rotation axis
c
y
x
{100}
{001}
{100}
lower
<010>
lower
<010>
upper

Figure 9

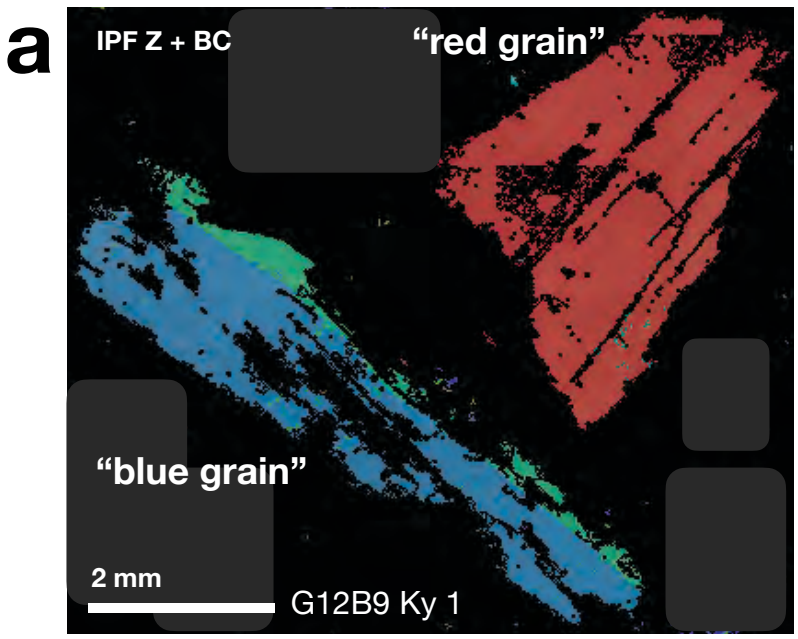
a
IPF Z + BC
"red grain"
"blue grain"
2 mm
G12B9 Ky 1

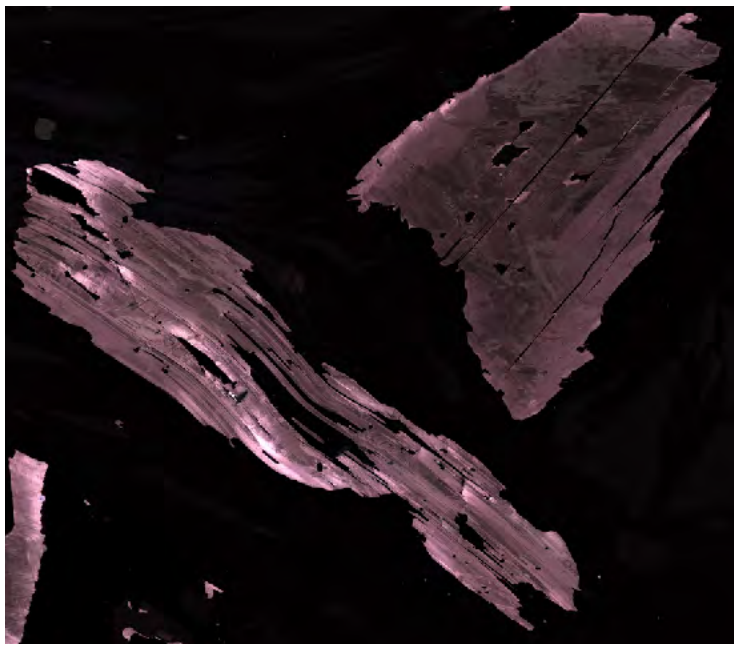
b

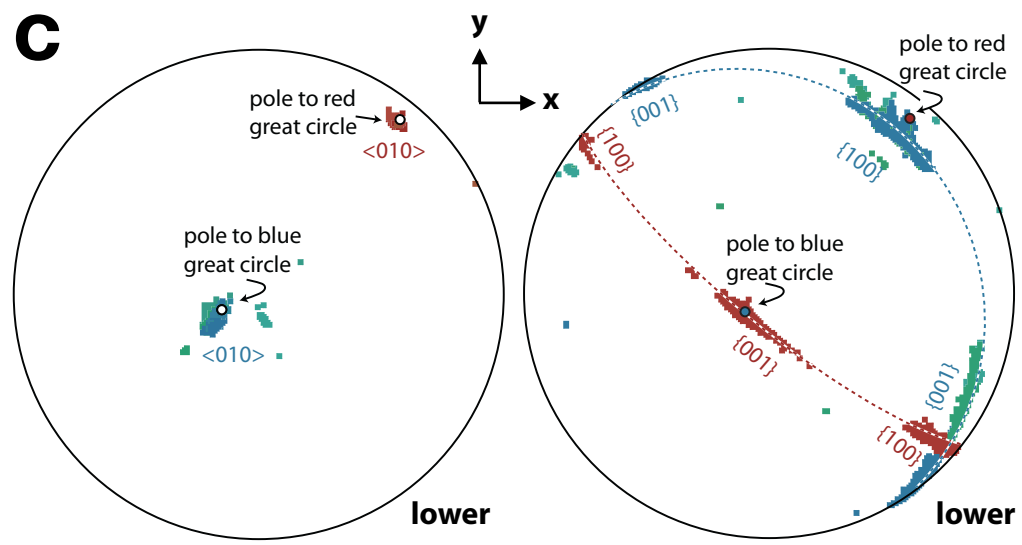
c
y
x
pole to red great circle
<010>
pole to blue great circle
<010>
lower
pole to red great circle
{001}
{100}
pole to blue great circle
{001}
{001}
{100}
lower

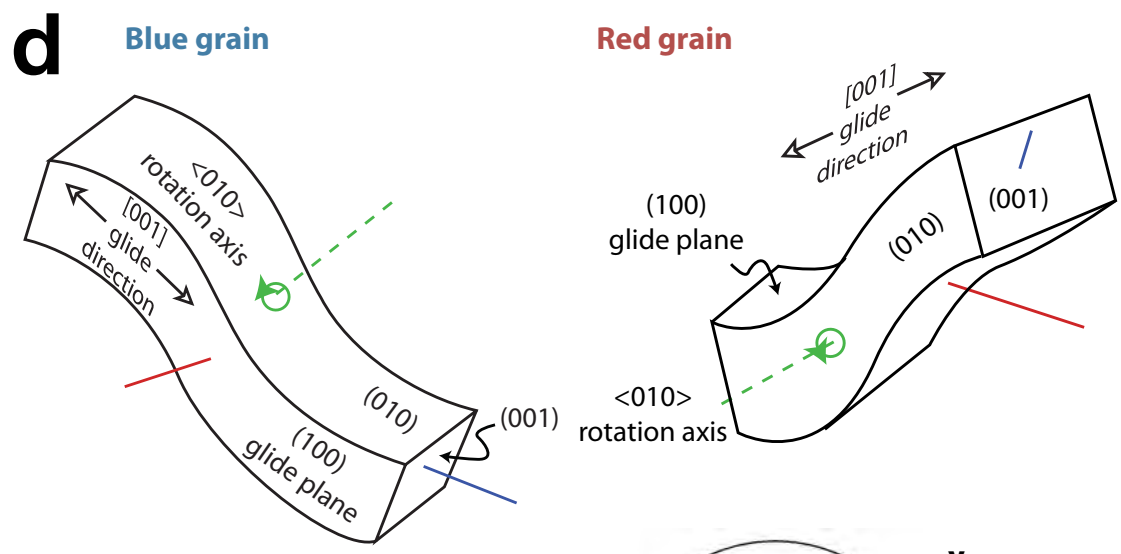
d
Blue grain
<010> rotation axis
[001] glide direction
(010)
(001)
(100) glide plane
Red grain
[001] glide direction
(100) glide plane
(010)
(001)
<010> rotation axis

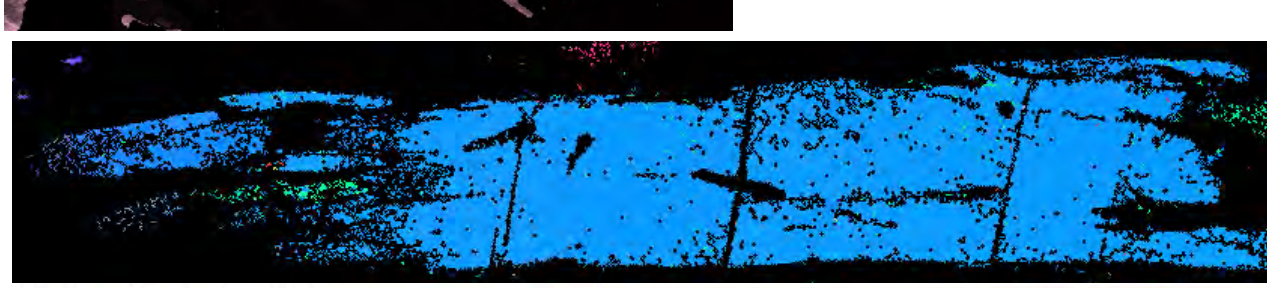
e

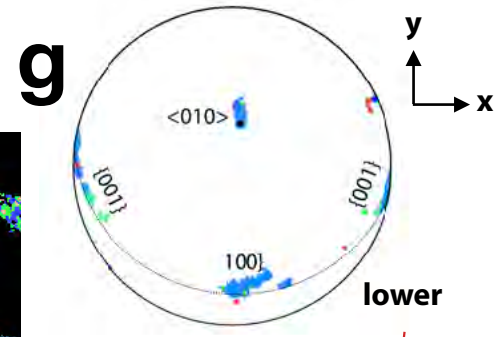
g
y
x
<010>
{001}
{001}
100}
lower

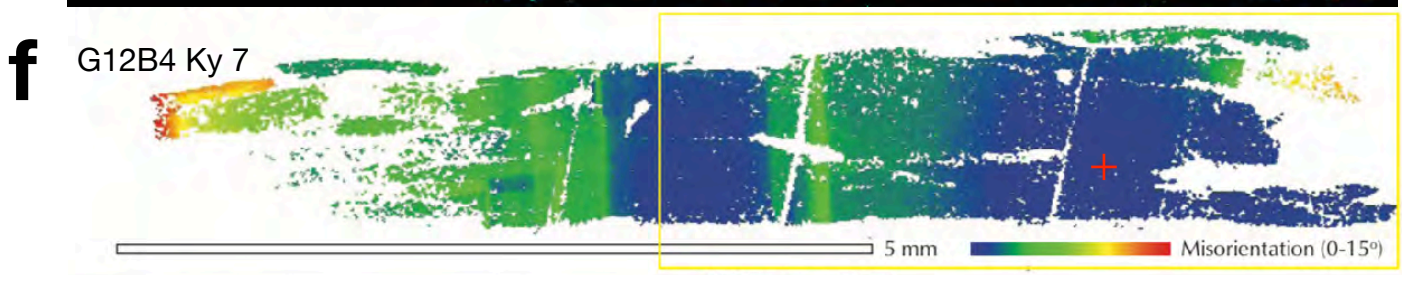
f
G12B4 Ky 7
5 mm
Misorientation (0-15°)

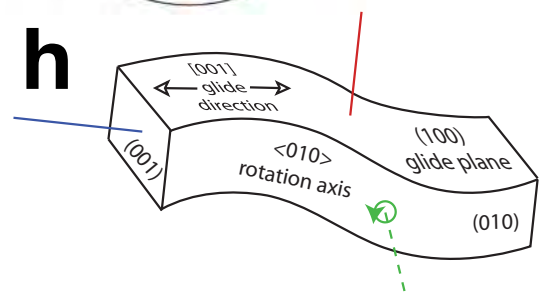
h
[001] glide direction
(001)
<010> rotation axis
(100) glide plane
(010)

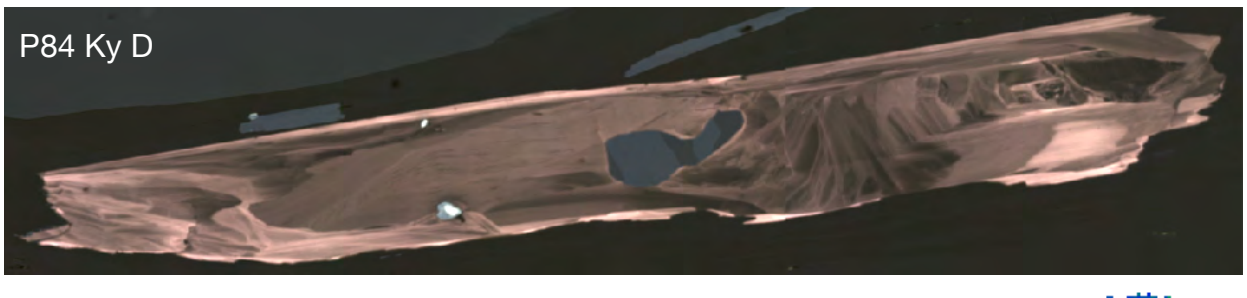
i
P84 Ky D

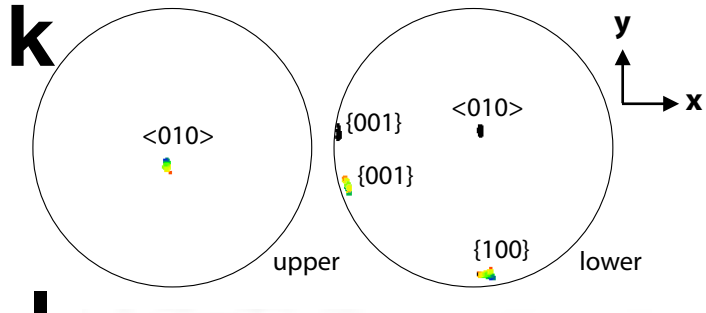
k
y
x
<010>
<010>
{001}
{001}
{100}
upper
lower

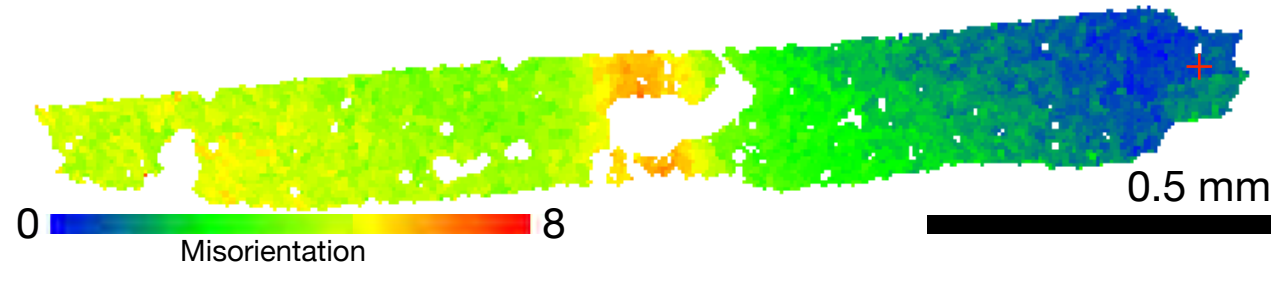
j
0
8
Misorientation
0.5 mm

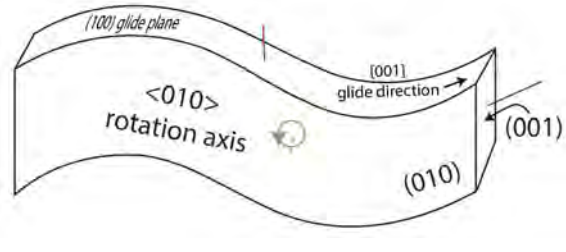
l
[100] glide plane
[001] glide direction
<010> rotation axis
(001)
(010)

beam conditions	*20kV*	*200nA*	*5um*
measured line	**Ti Kα**	**Zr Lα**	**Mn Kα**
monochromator	LPET+LPET	VLPET+VLPET	LLIF
count time (sec)	540	540	540
single point MDL (ppm)	1.6	5.9	4.4
precision 2σ (ppm)	2.4	9.0	6.7
beam conditions	*20kV*	*300nA*	*2um*
measured line	**Ti**	**Zr**	**Mn**
monochromator	LPET+LPET	VLPET+VLPET	LLIF
count time (sec)	600	600	600
single point MDL (ppm)	1.2	3.1	3.4
precision 2σ (ppm)	2.0	4.6	5.2

Cr Kα	S Kα	Ga Kα	V Kα	Cd Lα
LPET+LPET				
540				
1.8				
2.7				

Cr	S	Ga	V	Cd
LPET+LPET	VLPET+VLPET	LLIF	LPET+LPET	VLPET+VLPET
600	600	600	600	600
1.4	1.2	7.3	1.3	3.8
2.7	1.9	11.2	2.1	5.9

Ge Kα	Fe Kα	Mg Kα	P Kα
	LLIF	TAP	LPET+VLPET+VLPET
	540	540	540
	4.3	3.3	1.7
	10.3	5.6	3.1
Ge	**Fe**	**Mg**	**P**
LLIF	LLIF	TAP	LPET+VLPET+VLPET
600	563	563	563
9.3	3.4	2.6	1.3
14.1	7.3	4.1	2.0